Lithium extraction from clays and micas in the DAP well

BSc Thesis

F.W. Graveland

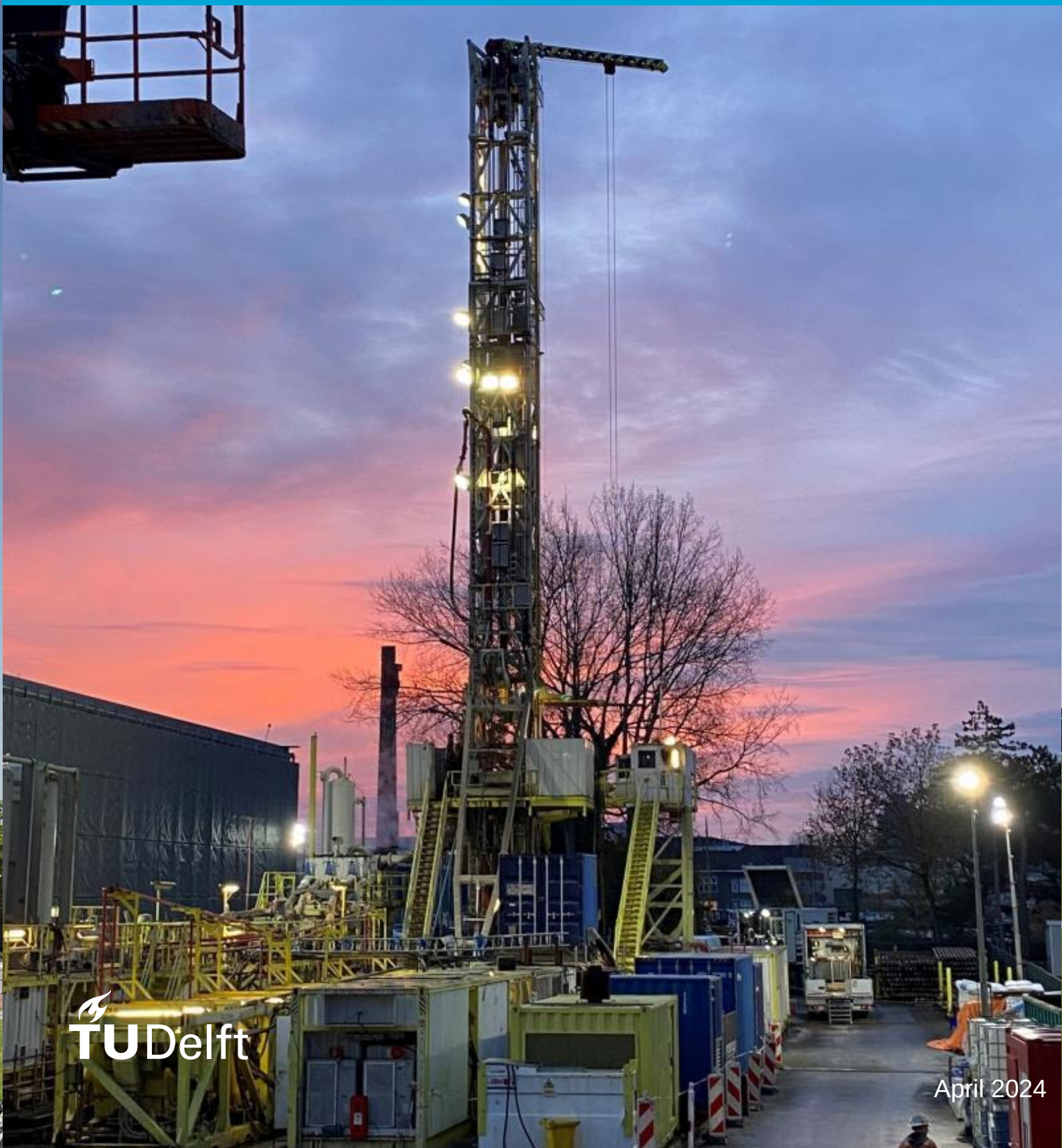

TU Delft

April 2024

Lithium extraction from clays and micas in the DAP well

By

F. W. (Femke) Graveland
5119715

Bachelor of Science
in Applied Earth Sciences

at the Delft University of Technology,
to be defended publicly on Thursday April 11, 2024, at 10:00 AM.

Supervisor:	Dr. T Schmiedel
Thesis committee:	Dr. H.A. Abels
	Dr. S.A. Jones

TU Delft

Abstract

The DAP well is a project by the TU Delft to be able to provide heat to a part of Delft. However, presently the geothermal well is not economically feasible. The well could be a potential source of lithium, which is mostly used in batteries. The demand for lithium is estimated to rise, thus this could potentially be a promising investment. In this research, the feasibility of extracting lithium from the clay and mica faces of the Delft Sandstone is estimated. The Delft Sandstone was formed in the Valanginian era and consists of sandstone and siltstone with clay interfaces. Potential minerals that could occur in this layer that can contain lithium are smectites, kaolinites, micas and illites, fibrous clays or chlorites. These minerals either contain lithium in their naturally occurring mineral structure or can be formed when in a mineral an element is substituted by lithium. The minerals that will be analysed in this research are hectorite, montmorillonite, bentonite, kaolinite, lepidolite, zinnwaldite, illite, sepiolite, palygorskite and cookeite. The samples will be analysed and interpreted using Gamma-Ray Spectroscopy and Infrared spectroscopy. Gamma Ray Spectroscopy detects the naturally occurring gamma rays emitted from a rock sample. These are quantified in a general signal as well as concentrations of Potassium, Thorium and Uranium. High clay content will relate to a high K value thus a high GR (Gamma Ray) signal. In IR (Infrared) Spectroscopy a beam of infrared light is passed through a sample, which leads to the absorption of specific wavelengths by the molecular bonds present. These spectra are then compared to library spectra and minerals can be identified. In this thesis, the GR signal could not be related to the well logs as the sample quantity was too low. From the IR Spectra kaolinite and illite were defined in this layer. These clays can contain lithium when elements are substituted in their molecular structure.

Contents

1 Introduction

There has been a high rise in the demand for lithium in the last decade (Figure 1) This is mainly due to the use of lithium-ion batteries (Figure 2) Lithium is the lightest and the most highly reducing of metals, which confers to high a volumetric energy density, which makes it very suitable for batteries (Peiró et al., 2013)

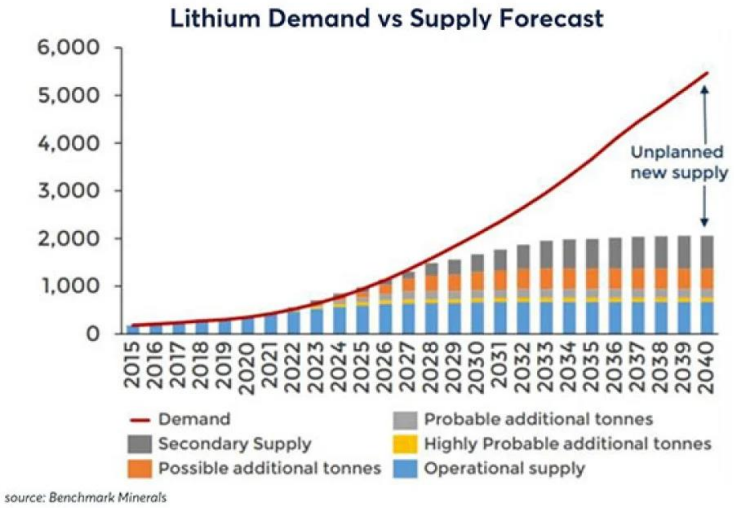

Figure 1: Lithium Supply and demand forecast (Capon, 2021).

As well as the use of lithium for lithium metal batteries and lithium-ion batteries, lithium is also used in the production of heat-resistant glass and ceramics, lithium grease lubricants, and flux additives for iron, steel, and aluminium production (Martin et al., 2017) (Figure 2) The demand is expected to rise even more, as the demand for electric vehicles and electronic devices also grows (Figure 1) To be able to meet climate goals set for the Netherlands, there is expected to be an increase in products such as hybrid and electric cars, permanent magnets for maglev trains, wind turbines and motors, and solar panels for which lithium is often used. The amount of lithium used for batteries is expected to increase between 30% and 60% (Peiró et al., 2013)

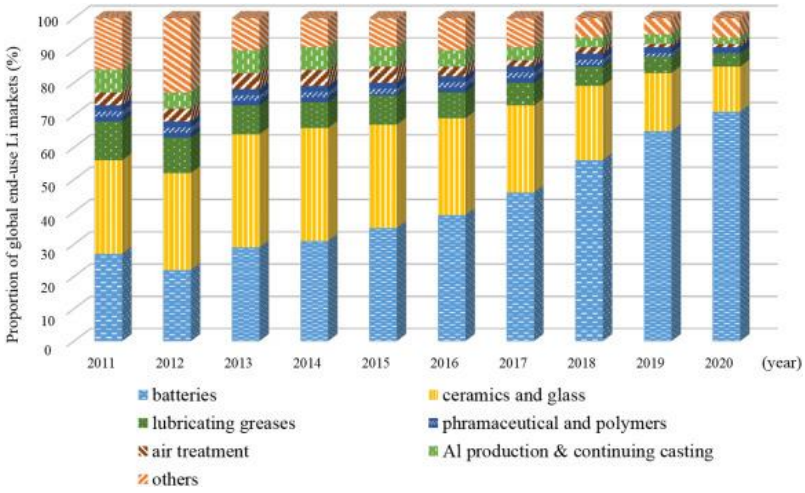

Figure 2: Lithium uses over the years (Zhao et al., 2023).

Presently, the major sources of lithium are brine lake deposits and pegmatites (Zhao et al., 2023) Pegmatites are coarse-grained igneous rocks formed by the crystallization of magma at depth in the crust. In brine lake deposits elements occur as ions in a dynamic fluid, instead of chemically bonded in a solid. Other potential sources of supply of lithium are clays and seawater (Kavanagh et al., 2018) Currently, there is also research being done on the potential to extract lithium from geothermal wells (Stringfellow & Dobson, 2021)

In Q4 of 2023, the Geothermal doublet was drilled on the campus of the Delft University of Technology. The well will eventually provide heat to the campus buildings and part of the city of Delft and thus be part of a larger initiative for the energy transition in the Netherlands (Master Plan Geothermal Energy in the Netherlands 2018). In addition, geothermal wells can be the source of (critical) raw materials, which are transported to the surface when dissolved in the geothermal fluids. Heat and extractable amounts of raw materials combined could increase the incentive for investors and financially de-risk geothermal projects in the Netherlands. Lithium is one of these raw materials investigated for potential extraction from geothermal fluids due to its cruciality for energy storage systems. However, many of the recent estimations and concentrations of raw materials do only consider fluid samples, whereas little is known about the source (minerals) for the Lithium in the geothermal reservoir. This study will investigate the cutting samples collected during the drilling process of the Geothermal campus well to identify phases which are potential Lithium sources. The focus will lie on the clay and mica phases of the geothermal reservoir, which will be characterized by a combination of spectral and element analytical methods consisting of differentiated Gamma-ray (GR) measurements and Infrared (IR) spectroscopy. The creation of a unique dataset like this will aid the predictability of element concentrations and help to better understand the long-term sustainability of Lithium and other metal ions and their variability in the Dutch geothermal brines. This is essential pre-knowledge for modern extraction technologies from fluids to be able to work since they are reliant on predictable and sustained concentrations.

This thesis aims to create an initial characterization of the spatial variability of different clay and mica phases in the Delft sandstone reservoir to provide potential sources for Lithium. It is expected that handheld gamma-ray measurements on samples of rock cuttings can provide overall trends similar to the more expensive high-resolution well logs. Subsequently, this research will attempt to determine the potential phases of clay and micas containing Lithium that can be found in this reservoir using Infrared spectroscopy. It is estimated that there will be clay minerals present that have to ability to contain lithium.

2 Background

2.1 Geology

In this research samples from the Delft Sandstone layer are examined. The Delft Sandstone layer is located in the West Netherlands basin (Figure 3).

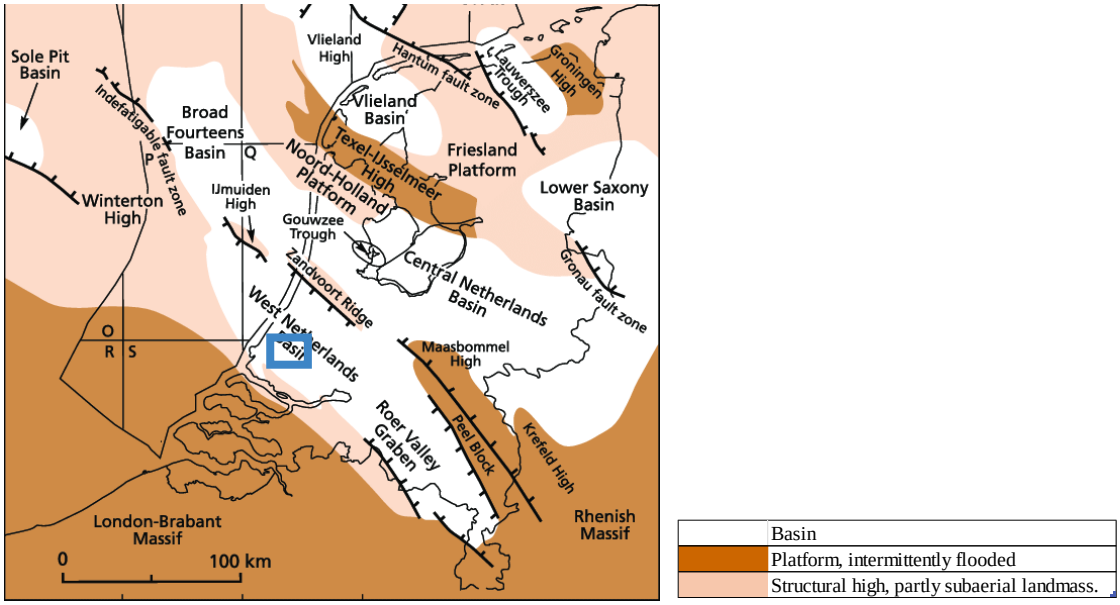

Figure 3: Map of Late Jurassic to Early Cretaceous structural elements in the Netherlands. Delft indicated by the blue square (after Van Adrichem 1933).

The Delft Sandstone is part of the Nieuwekerk formation which consists, from base to top of the Alblasserdam Member, the Delft Sandstone Member, and the Rodenrijs Claystone Member (Figure 4). The Nieuwekerk formation was formed from fluvial succession during and after a major Early Cretaceous rifting phase in the West Netherlands Basin. The thickness of the Delft Sandstone Member varies between 0 and 130 meters. In the DEL01 well, the layer is estimated to lie between 2735- and 2867-meters depth (Geothermie Delft & Geo Service GMBH, 2023). The Delft Sandstone layer is classified as Valanginian in age (Donselaar et al., 2015).

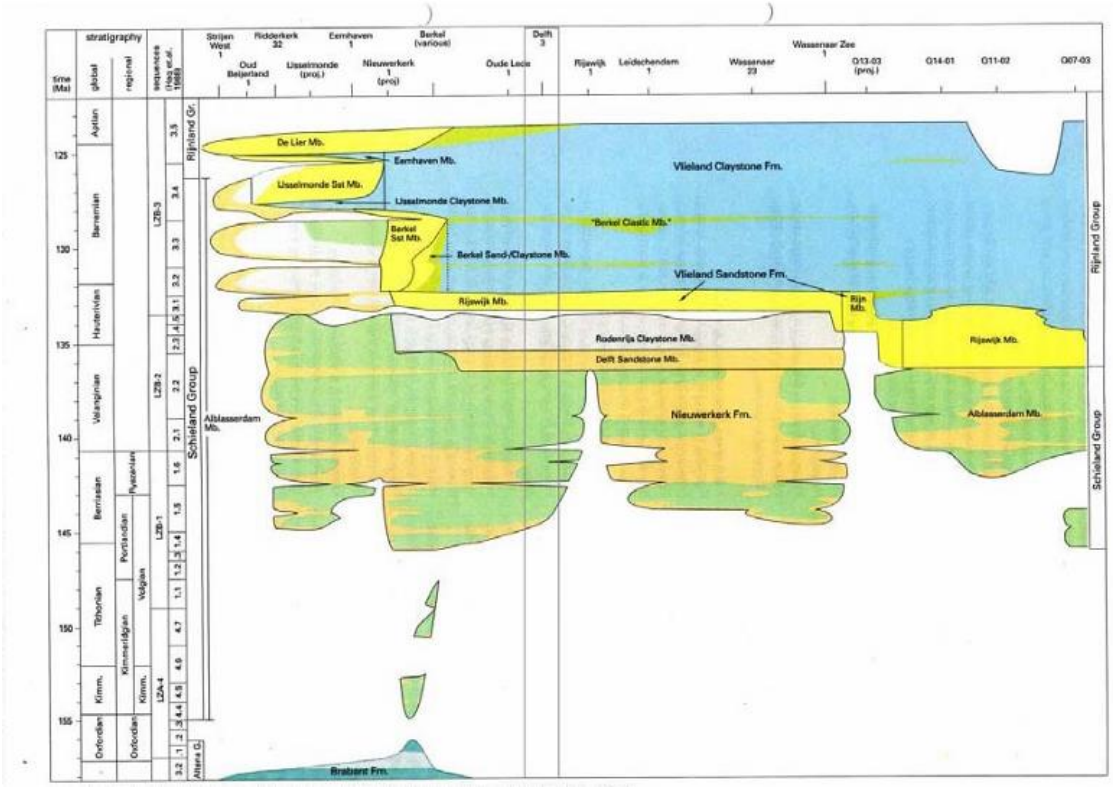

Figure 4:Figure: Litho-chronostratigraphic section through the West Netherlands Basin with the Delft Sandstone. The area of the DAP well is marked by a rectangle (van Adrichem Boogaert & Kouwe, 1933).

The Delft Sandstone can be divided into three subsections (Table 1) (Donselaar et al., 2015). These sections can be related to the lithographic descriptions mentioned in the well-log report (Table 1).

Unit	Depths [m MD]	Description Well Log Report
3	2822-2868	***Sandstone**, loose, colourless dull to milky, also clear, fine to medium grained, poorly sorted, subrounded to rounded; siltstone light grey to dark grey friable to firm; Acc.: Mica*
2	2798-2822	***Siltstone**, off-white, brownish white, friable, crumbly, sandy, and subordinated claystone, medium to dark grey, silty, platy, moderately hard, as well as sandstone, light grey, grey, white, fine to coarse-grained, poorly sorted; quartz grains milky to clear, subrounded to rounded in a silty matrix. Acc.: Mica*
1	2708-2798	***Sandstone**, milled to lose grains, white to off white, fine to coarse grains, subrounded to rounded, poorly sorted, milky to rarely clear in alternated layers with silty claystone, grey to darkish grey, firm to hard, partly platy, flaky. Siltstone, grey, light grey, white grey, friable to hard. With interbedded coal.*

Table 1: Lithographic descriptions of the different units in the Delft Sandstone with the depths (Geothermie Delft, 2023).

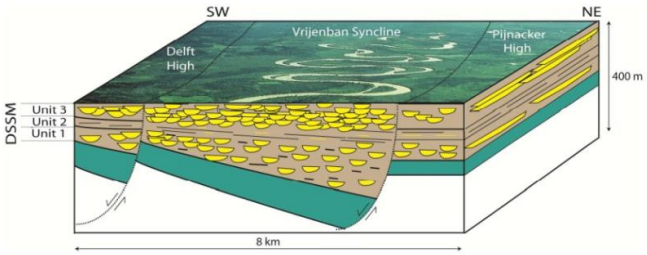

Figure 5: Figure: Depositional model of the Delft Sandstone layer with the different units marked (Donselaar et al., 2015).

These three sections are also described by Donselaar, Groenenberg & Gilding (2015) in Figure 5 The deposition of the lowest (oldest) layer occurred during a period of active faulting and rise of sea level. This resulted in a high rate of accommodation space increase. The deposits of this period consist of loosely stacked meandering river sandstone bodies with well-preserved fine-grained tops embedded in a floodplain claystone and siltstone matrix (Donselaar et al., 2015).
During the deposition of the middle section, the continued relative sea level rise led to a temporal lack of course-grained fluvial sediment supply to the area. The deposits of this period are extensive fine-grained floodplain and swamp sediments with an overall low net sand content consisting of interbedded claystone, siltstone, and coal layers.
When the top section was deposited relative sea level rise decreased and led to the deposition of laterally amalgamated and vertically stacked fluvial sandstone bodies with minor mudstone floodplain intervals (Donselaar et al., 2015).

2.2 Minerals

Presently, lithium is mostly extracted from hard rocks and brines. However, lithium can also be present in clays and micas. This can happen in smectites, kaolinites, micas, illites, or chlorites (Starkey, 1982). The exaction of lithium for clay is a relatively new method, accounting for 8% of the lithium resources (Ashby, 2016). In Figure 6 an overview is given of current sources of lithium extraction per country.

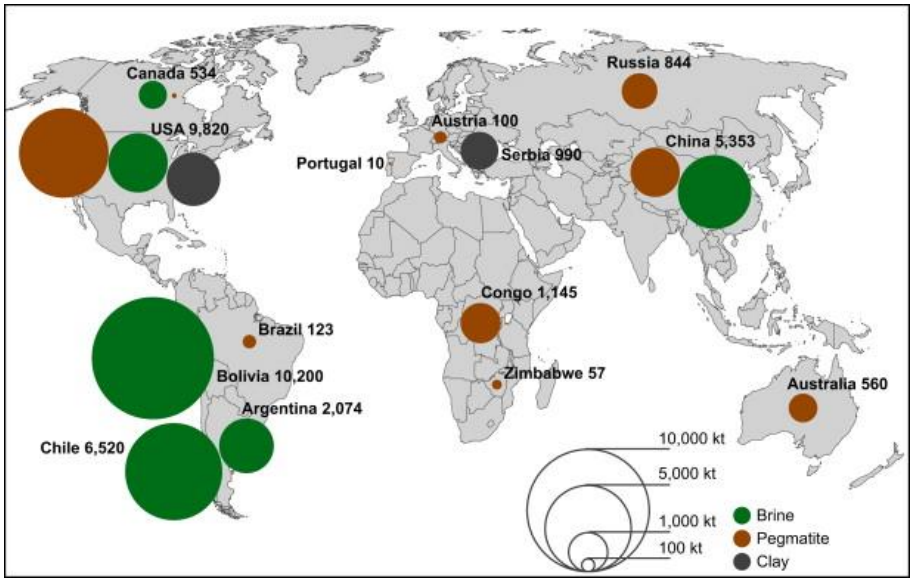

Figure 6: Lithium resources (in thousand tons) by country and deposit type (Ashby, 2016).

2.2.1 Mineral structures

The Li-bearing clay minerals that are observed in this research are phyllosilicates and are of microscopic sheets composed of Fe, Li, Ca, Na, Mg, K, Si, Al, O, and/or OH, and inter-layer spaces. (Grant et al., 2020).These layers consist of tetrahedral sheets and octahedral sheets ((Figure 7). They can be structured as a 1:1 layer of one tetrahedral sheet and one octahedral sheet or a 2:1 layer with two tetrahedral sheets and one octahedral sheet (Figure 7c) (Zhao et al., 2023). The lithium can either be present within the framework sheet structure of the mineral or in the interlayer spaces between the sheets (Grant et al., 2020).

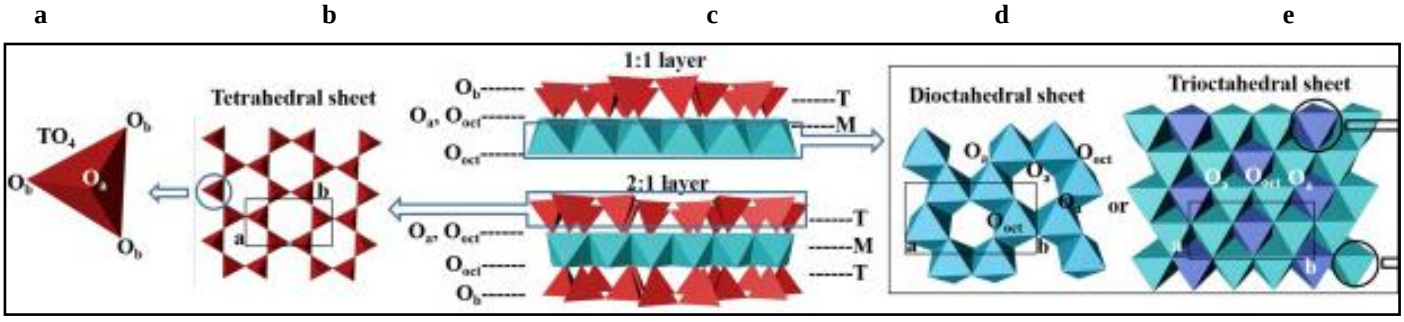

Figure 7: Figure 1: (a) a tetrahedron (b) a tetrahedral sheet; (c) models of a 1:1 and 1:2-layer structure (d) a dioctahedral sheet; (d) a trioctahedral sheet.

2.2.2 Smectites

Smectites are made up of two silica tetrahedral layers which are electrostatically cross-linked via an Al_2O_3 or Fe_2O_3, octahedral central layer. These layers are not rigidly connected but are separated by a free space. In this interspace, cations can occur. The lithium content in smectite clays can vary depending on the source of the clay and the presence of other minerals during formation. Trioctahedral smectites (Figure 7e) can contain the largest amounts of lithium; dioctahedral smectites (Figure 7d) generally contain less (Starkey, 1982). Hectorite is a part of the trioctahedral smectite group. In this mineral, Li^+ can be in the octahedral layer indicated with blue or in the interspace indicated by white in Figure 8 (Zhao et al., 2023). Next to hectorite, other lithium-bearing smectite clays are montmorillonite, swinefordite and bentonite. These clays have a similar layered structure with a high surface area and cation exchange capacity, which makes them very suitable for adsorbing lithium ions. Lithium-bearing smectites can be formed by hydrothermal alteration or precipitation in high-alkali lacustrine deposits (Starkey, 1982). This means forming these smectite clays requires specific conditions such as sedimentary basins where volcanic ash has been deposited and subsequently altered by chemical weathering processes.

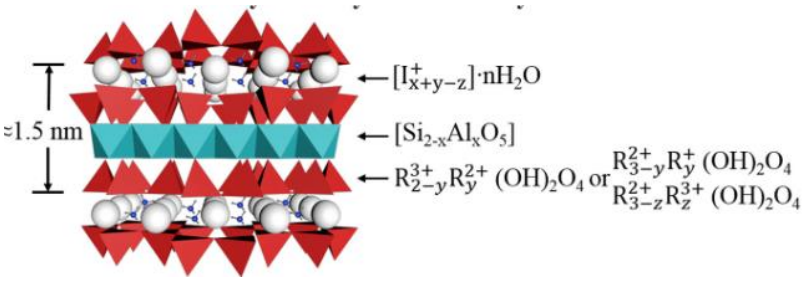

Figure 8: : The 2:1 layer structure of hectorite with 2 tetrahedral sheets (red), 1 octahedral sheet (blue) and hydrated interlayer cations (white) (Zhao et al., 2023).

2.2.3 Micas

Lithium is often found in micas. Micas can be described by the general formula $AB_{2-3}(X, Si)_4O_{10}(O, F, OH)_2$, where the B can be substituted by lithium (Deer, Howie, Zussman, 1966). They are composed of an octahedral cationic layer sandwiched between two identical tetrahedral layers (Figure 9) (Zhao et al., 2023). The most occurring micas that have lithium in their molecular structure are lepidolite and zinnwaldite (Li et al., 2019). In these minerals, the Li^+ ion can reside in the octahedral layer or the interspace (Zhao et al., 2023). Lepidolite and zinnwaldite tend to occur in evolved granites and pegmatites (Alderton, 2021).

Lithium can also be present in micas that do not contain lithium in their framework structure such as illite, when the ions Mg^{+2}, Fe^{+2}, or Al^{+3} in the interspace are substituted for lithium ions. However, illite has limited interlayer space and therefore exhibits less cation exchange capacity when compared to other clays, such as smectites (Figure 10). Illite is formed by the alteration of clay minerals, clastic feldspars, and rock fragments (Wang et al., 2022). Illite can contain lithium in environments where lithium-bearing micas or clays weather and lithium ends up in the water and is incorporated into the structure of newly formed clay minerals (Starkey, 1982).

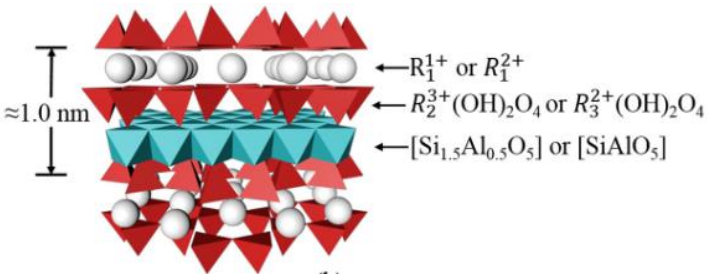

Figure 9: The 2:1 layer structure of lepidolite and zinnwaldite with 2 tetrahedral sheets (red), 1 octahedral sheet (blue) and interlayer cations (white) (Zhao et al., 2023).

2.2.4 Kaolinites

Kaolinites are clay minerals that do not contain lithium in their molecular structure but can contain lithium as impurities. Kaolinites have a 1:1 layer structure (Figure 7c top) and are made of one tetrahedral Si_4O_{10} sheet and one octahedral aluminium hydroxyl sheet (Król-Morkisz & Pielichowska, 2019). When magnesium substitutes for aluminium, a charge deficiency is created that is satisfied when a lithium-ion moves into one of the vacant octahedral spaces (Starkey, 1982). Kaolinite is formed by the decomposition of other aluminosilicates, especially feldspars by weathering and/or hydrothermal activity in acid igneous rocks (King, 2009).

In Figure 10 a model of the different mineral structures of kaolinite, smectite and illite is shown.

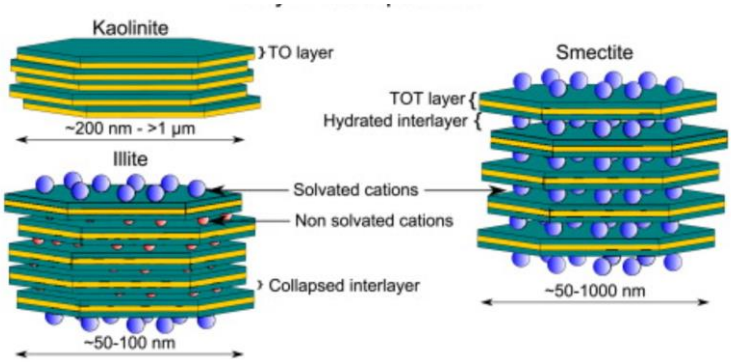

Figure 10: Structure of the layers of kaolinite, illite and smectite.

2.2.5 Chlorite

The last type of potential lithium-bearing minerals in this thesis is the chlorite group with general formula $(Mg,Fe)_3(Si,Al)_4O_{10}(OH)_2\cdot(Mg,Fe)_3(OH)_6$. Cookeite is an example of a chlorite-type mineral that can contain lithium. This mineral has a 2:1 interlayer structure with a di-trioctahedral layer (Figure 11) (Zhao et al., 2023). The Li^+ ion is usually located in the dioctahedral layer when Si^{4+} is replaced by Al^{3+} in the tetrahedral layers and a charge deficiency is created that can be satisfied by Li^+. Cookite is formed as an alteration mineral in lithium-rich granite pegmatites (Zhao et al., 2023).

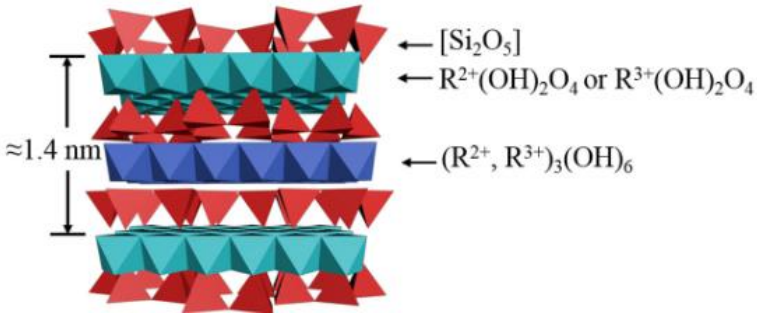

Figure 11: The 2:1 layer structure of cookeite with 2 tetrahedral sheets (red), 1 octahedral sheet (light blue) and octahedrally coordinated cations in the interlayer (dark blue) (Zhao et al., 2023).

2.2.6 Extraction

The problem with mining lithium from clay minerals is that with present technology the extraction is not economically feasible due to high reagent consumption and energy costs when compared to extracting it from brines and pegmatites (Li et al., 2019). However, lime–gypsum roasting-water leach seems to be the most promising. This method involves mixing lithium-bearing clay, gypsum ($CaSO_4 \cdot 2H_2O$) and limestone ($CaCO_3$) and roasting them at elevated temperatures of around 1000 °C. Afterwards, these roasted samples are water-leached to dissolve lithium (Büyükburç et al., 2006).
Another method could be a chemical reaction between the sedimentary clay mineral and NaCl, which modifies or degrades the framework layer structure and frees lithium. This method can be used when the lithium is mobile and is found in the interlayer. (Grant et al., 2020).
An applicable method when the lithium resides in the framework layer could be a process that swaps the lithium for a sodium ion trough ion exchange. In this case the product would be a LiCl solution and a clay where minimal modifications to the framework layer were made. (Grant et al., 2020).

2.2.7 Overview

An overview of all minerals that can contain lithium can be found in Appendix 1. The minerals that will be used in this thesis are summarised in Table 2. In clays that do not contain lithium in their chemical formula, lithium can replace magnesium, ferrous iron, or aluminium in silicates and aluminosilicates.

Mineral	**Formula**
Hectorite	$Na_{0.3}(Mg,Li)_3Si_4O_{10}(OH)_2$
Montmorillonite	$(Na,Ca)_{0.33}(Al,Mg)_2(Si_4O_{10})(OH)2{\cdot}nH_2O.$
Swinefordite	$Li(Al,Li,Mg)_3((Si,Al)_4O_{10})_2(OH,F)_4 \cdot nH_2O$
Bentonite	$Na_{0,5}Al_{2,5}\ Si_{3,5}O_{10}(OH)_2{\cdot}(H_2O)$
Kaolinite	$Al_2Si_2O_5(OH)_4$
Lepidolite	$K(Li,Al)_3(Al,Si,Rb)_4O_{10}(F,OH)_2$
Zinnwaldite	$KLiFeAl(AlSi_3)O_{10}(OH,F)_2$
Illite	$(K,H_3O)(Al,Mg,Fe)_2(Si,Al)_4O_{10}[(OH)_2,(H_2O)]$
Sepiolite	$Mg_4Si_6O_{15}(OH)_2{\cdot}6H_2O$
Palygorskite	$(Mg,Al)_2Si_4O_{10}(OH){\cdot}4(H_2O)$
Cookeite	$LiAl_4(Si_3Al)O_{10}(OH)_8$

Table 2: Potential lithium bearing minerals used in this thesis.

2.3 Gamma Ray

The first method used in this project is Gamma-ray (GR) spectroscopy. This tool detects the naturally occurring gamma rays emitted from a rock sample (Serra et al., 1980). Gamma rays are high-energy photons which are emitted during the decay of atomic nuclei. The spontaneous decay of radioelements leads to the emission of alpha, beta, and/or gamma radiation depending on the decaying element. All three radiations may be of interest in laboratory investigations, but only gamma rays penetrate rock and air sufficiently to allow practical geophysical measurements (Horwood, 1961). Gamma rays have frequencies greater than 1019 Hz, wavelengths less than 10−12 m, and have energies above 104 eV (McCay et al., 2014). The gamma-ray measures the presence of the elements Potassium [40K], Uranium [238U], and Thorium [232Th] as they emit characteristic gamma-ray radiation during decay. The concentrations of these elements increase with silica content (McCay et al., 2014). Radio elements are naturally present in most rocks, however in certain types of rock are concentrated at higher levels. Clay minerals are known to possess distinct gamma-ray signatures due to their elemental composition.

The GR signal is expressed in API (American Petroleum Institute) units or CPS (Counts Per Minute), K is expressed in % and Th and U are expressed in ppm (Serra et al., 1980). The first radioactive isotope measured is potassium [K-40]. Potassium emits gamma rays with characteristic energies of 1.46 MeV. Thorium and Uranium are detected by their daughter product, 214Bi (1.76 MeV) for uranium and 208Tl (2.62 MeV) for thorium, as these products emit a relatively larger energy signature when compared to the signatures of uranium and thorium and thus can be easier distinguished. Consequently, uranium and thorium concentrations are displayed as equivalent uranium (eU) and equivalent thorium (eTh) (McCay et al., 2014).

Gamma-ray spectroscopy is a non-destructive method to measure these gamma-ray signals.
A gamma-ray spectrometer can detect the interaction of a photon with a medium in one of three ways: photoelectric absorption, Compton scattering, or pair production. However, these photons are only visible to a detector if they interact with a medium. Therefore, a gamma ray spectrometer needs to, next to being able to accurately detect the electrons that are created, function as a medium that will have a high chance that an incident gamma-ray will interact with it (Rittersdorf, 2007).

2.3.1 Photoelectric absorption

In the equipment used in this research, the method of photoelectric absorption is used (SatisGeo, 2015). During this process ionising radiation interacts with matter, and the electrons within the molecules get excited by the energy from the radiation to a higher energy state. Next a photoelectron is produced from one of the electron shells of the absorber and energy is released when the electrons return to their ground state. This interaction releases kinetic energy that can be estimated with Ee− = hv− Eb, where Eb is the binding energy of the freed electron in its original shell (Rittersdorf, 2007). The electron's energy can be described as the difference between the x-ray photon energy and the energy needed to remove the electron from the atom. The process of visible light being created from photoelectric absorption is called scintillation (Bronzino, 2012).

2.3.2 Equipment

The equipment used in this research for gamma-ray detection is the SatisGeo GS-512i Portable Gamma Ray Spectrometer. This equipment is developed for gamma-ray measurements done in the field and is made to be used on surface soil layers of 2-20 cm thickness (SatisGeo, 2015).

The SatisGeo GS-512i Portable Gamma Ray Spectrometer is a scintillation NaI (Tl) 76x76 mm detector (SatisGeo, 2015). The scintillator produces a pulse of light when the gamma ray interacts with the crystal composed of thallium activated NaI crystals. NaI is used as it is well characterized, provides a good gamma ray resolution and is relatively cost-efficient. Furthermore, the high atomic number for iodine in NaI(Tl) gives a good efficiency for gamma-ray detection. The thallium is added to ensure that the scintillation photons are not reabsorbed by the crystal by shifting the wavelength of the photon (Firestone, 2005). This pulse is then converted into an electric pulse by a photomultiplier tube which consists of a photocathode, a focussing electrode and several dynodes that multiply the number of electrons striking them. Lastly, the anodes and dynodes are biased by a chain of resistors. An example of a scintillation gamma ray detector is shown in figure 12 (Firestone, 2005).

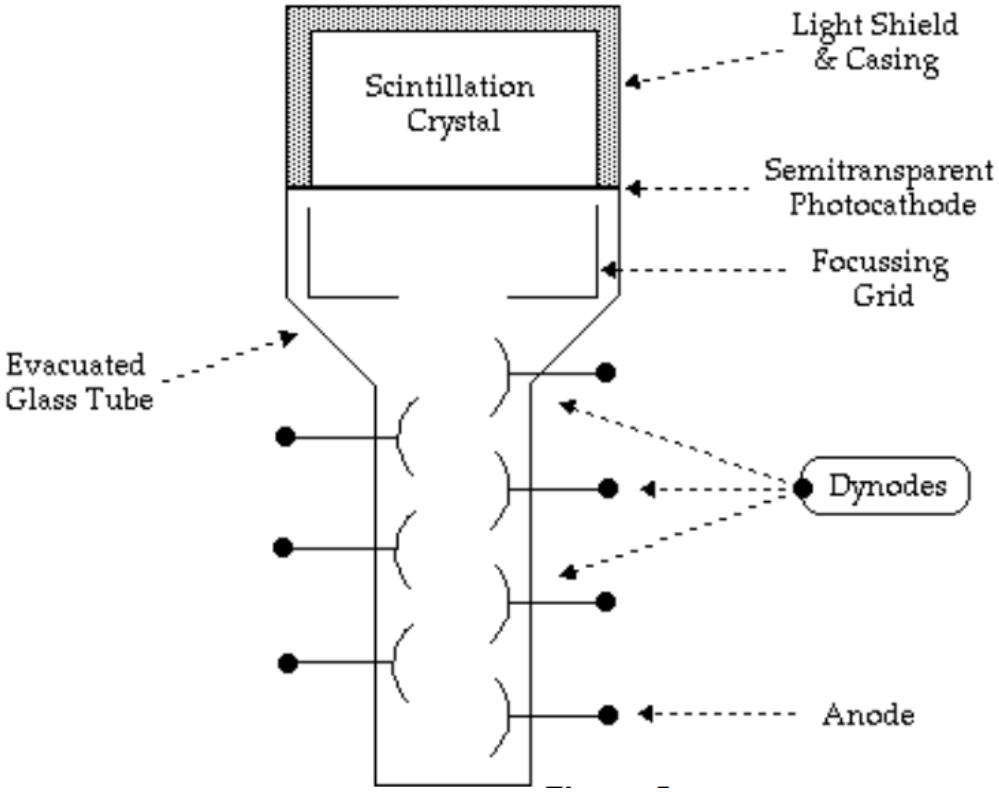

Figure 12: Scintillator Gamma Ray detector.

These electric signals consist of voltage pulses where the amplitude of the pulses is proportional to the energy of gamma quanta. These pulses are then separated into channels that correspond to the given energy of gamma radiation by a pulse amplitude analyser (SatisGeo, 2015).

The spectrometer returns values of K, Th and U and a plot. In Figure 13 an example plot is shown as well as an interpretation of the peaks.

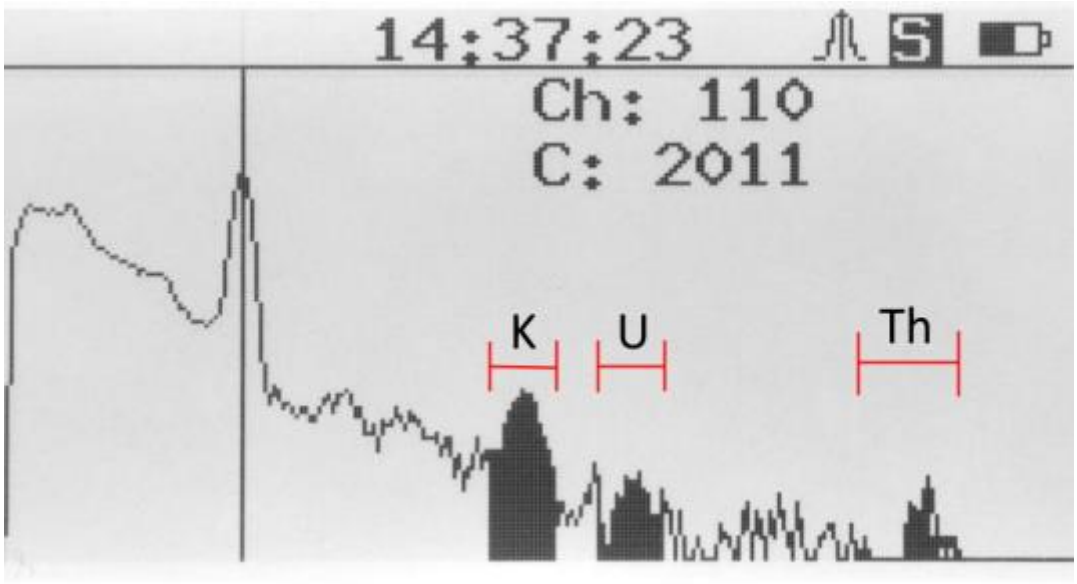

Figure 13: Example of display of GS-512i Portable Gamma Ray Spectrometer with peaks indicated.

2.3.3 Interpretation

As mentioned previously the Gamma Ray can be used to detect silicates as silicates have a specific grain size and mineralogical composition. Clays are characterized as materials with a main mineralogical composition of phyllosilicates, and a grain size that is among the smallest of the granular lithologies. Because of the small grain size, the clays have low resistivity. The mineralogical composition has high potassium content and thus causes high K values, and this causes a high gamma-ray signal (Díaz-Curiel et al., 2021). In most clays, the concentrations of uranium and thorium are similar to other sediment types. Clays can thus be recognized by a high peak in K value.

2.4 Infrared Spectroscopy

Infrared Spectroscopy is a tool to investigate clay minerals' structure, bonding, and chemical properties such as mineral species, abundance, and crystallinity (Xu, et al., 2001). It is a practical tool in the identification of clay minerals as the sample preparation is relatively easy and fast, only requires a small sample quantity, and the method is non-destructive (Tóth, et al., 2012).
During IR spectroscopy, a beam of infrared light is passed through a sample, which leads to the absorption of specific wavelengths by the molecular bonds present. The molecules in the sample consist of atoms held together by chemical bonds. These bonds can stretch, bend, or rotate in various ways. When a molecule absorbs infrared radiation, it changes these vibrational modes (Ritz et al., 2011). Each type of bond has characteristic vibrational frequencies at which it absorbs infrared radiation. Clay minerals exhibit characteristic absorption bands corresponding to molecular vibrations in the mid-range of the infrared. Clay minerals have characteristic absorption bands that can be related to the fundamental stretching (ν) and bending (δ) vibrations of their basic functional groups (Madejová, et al., 2017).

2.4.1 Identification

These spectral features serve as diagnostic markers for differentiating clay mineral species. The intensity and position of absorption bands provide qualitative information about mineralogy and structural properties. Identifying clay minerals via IR spectroscopy involves comparing experimental and reference spectra of known minerals. Mineral identification is based on wavelength positions, intensity and shape of absorption troughs, and the overall shape of the entire spectrum. In Figure 14 an example of several spectra is given as well as their characteristic absorption and their meaning. In this research, the VNIR/NIR/SWIR (Very Near Infrared/Near Infrared/Short Wave Infrared) range is measured (Laukamp, et al., 2021.).

This range is chosen as in this range distinct spectral absorption features of clay minerals can be observed. The most relevant information for the detection and quantification of clay mineral content can be observed in the 1800–2000- and 2150–2250-nm regions which correspond to the bound water in the clay lattice interlayer and the Al–OH combination band, respectively (Goetz et al., 2001). When using equipment that has a higher spectral range, such as FTIR, features of carbonates, sulphates and quartz can be defined (Laukamp, et al., 2021). However, for this thesis, the 350-2500 nm range is enough to be able to identify clay minerals.

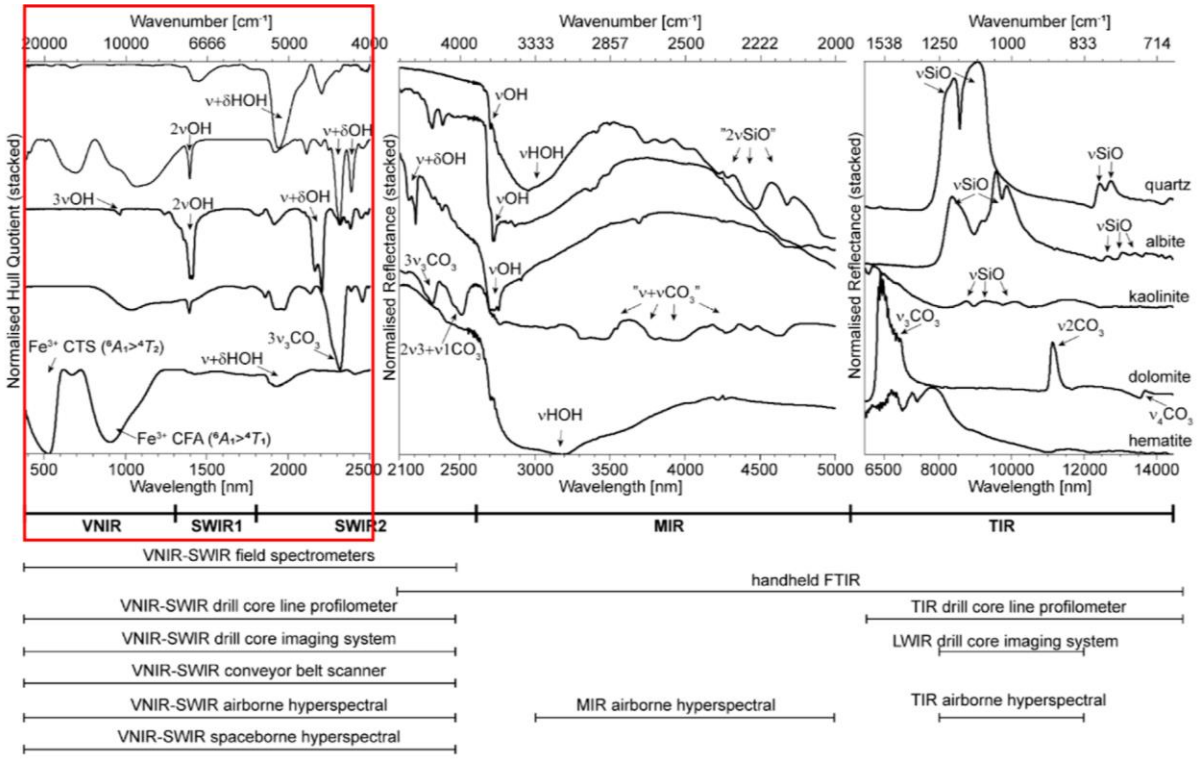

Figure 14: The reflectance spectra of major rock-forming minerals in the 380 to 14,500 nm wavelength region, the range used in this thesis is indicated by the red box (Laukamp, et al, 2021).

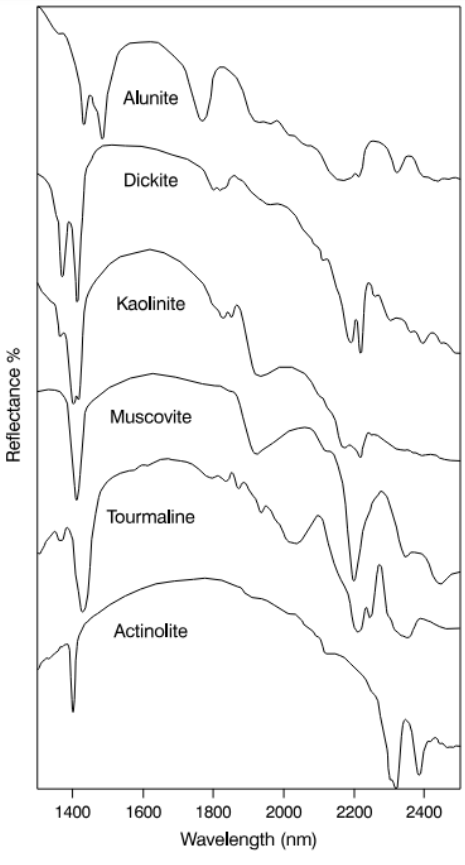

Each clay mineral displays a unique fingerprint spectrum, allowing identification based on the positions and intensities of characteristic absorption bands. The first absorptions in sheet silicates caused by the overtones of fundamental stretching vibrations of hydroxyl groups (2vOH), are located between 1390 and 1445 nm. These absorptions of sheet silicates that could contain lithium are shown in Figure 16 (Laukamp, et al, 2021). However, not only the wavelengths but also the shape of the absorption absorptions should be considered for identifying minerals. For example, kaolinite in Figure 15 exhibits distinct absorptions at around 1412 nm caused by double OH absorption (AusSpec International, 2008). The first absorption of muscovite and dickite are approximately at the same wavelength, however, in dickite a distinct double absorption can be observed, while in the muscovite spectrum, a single absorption can be observed. In the kaolinite spectrum, there is a very shallow double absorption present. By looking at the wavelengths and the shape of the absorption identification can be done.

Figure 15: Spectrum of different minerals. (Thompson et al., 1999).

Mineral Group	Mineral Species (Examples)	Assignment of Absorption	Lower Limit (nm)	Upper Limit (nm)
sheet silicate	kaolinite	2vMnOH	1392	1415
sheet silicate	lepidolite		1387	1425
sheet silicate	smectites		1394	1445
sheet silicate	Palygorskite		1386	1443
sheet silicate	chlorite		1391	1415

Figure 16: Sheet silicates with their first characteristic peak (Laukamp, et al, 2021).

2.4.2 Crystallinity

From the IR spectrum estimations of crystallinity as well as origin of the mineral can also be done. Highly crystalline kaolinites, for instance, give sharper more defined absorptions (Laukamp, et al., 2021). From these crystallinity interpretations assumptions can be made about the origin of the clay using the kaolinite cycle as shown in Figure 17 (AusSpec International, 2008).

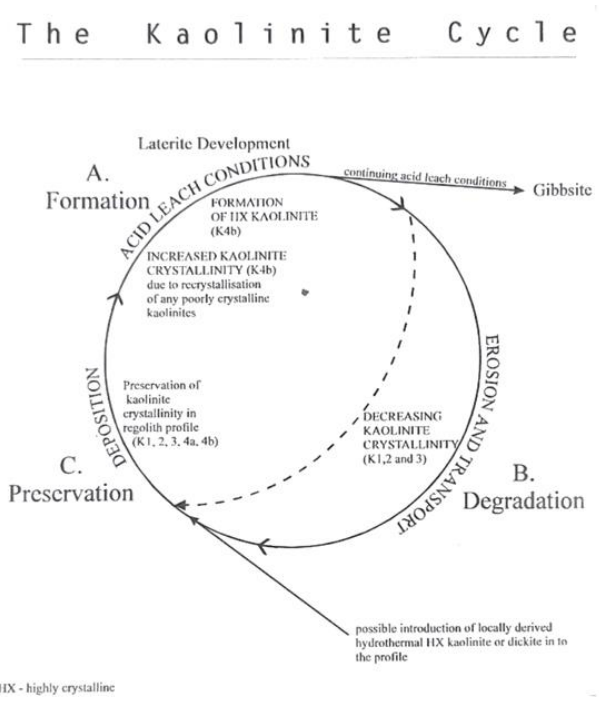

Figure 17: The kaolinite cycle (AusSpec International, 2008)

2.4.3 Equipment

In this research, a near-infrared spectrometer is used to generate the VNIR/NIR/SWIR spectrum. The ASD FieldSpec 4 Hi-Res NG Spectroradiometer is used. The spectral range of this device covers wavelengths between 350 and 2500nm and the sampling rate is 0.2.
seconds per spectrum. The device uses three different detectors to facilitate the recording of the spectra. For the VNIR (350-1000nm) region it uses a silicon-photodiode-array composed of 512 elements. For the SWIR1 (1000-1800nm) and the SWIR2 (1800-2500nm) region it used thermoelectrically cooled InGaAs-photodiodes (Indium, Gallium, Arsenid) Danner, et al., 2015). The spectral resolution of the FieldSpec 4 device is 3 nm at 700 nm, 6 nm at 1400 nm and 6 nm at 2100 nm (Malvern Panalytical, 2024).

3 Methods

The method of this research consists of 3 steps: preparation of the samples, GR- spectroscopy and ASD.

3.1 Preparation of the samples:

First, the full range of the DEL-GT-01 well samples (depths 2285-2930 mMD) was subsampled (available through: https://www.tudelft.nl/citg/over-faculteit/afdelingen/geoscience-engineering/research/geothermal/geothermal-science-and-engineering/research/campus-geothermal-project/sample-and-data-access). This was done by weighing each sample before the subsampling. Then, if the original sample was less than 80 grams no subsample was taken. If this sample was more than 75 grams a subsample of approximately 27 grams was taken. The containers in which the subsample was stored weighed about 12,7 grams and these containers were filled up until they weighed 40 grams. The containers were also marked with the sample number, the well number, the depth at which the sample was taken, and the time at which the sample was taken. If the sample was not enough or not present this was noted down and put in the GTD documentation.

During drilling CaCO3-mud additives were added (Appendix 2)(Halliburton, 2023). However, because the carbonate-rich drilling fluids can influence the ASD signal this had to be removed. To eliminate these drilling fluids, hydrochloric acid was applied to the samples.
In the first test, two samples of 28 grams were used from a similar well. One sample was mixed with 10 mL 0,5 molar HCl and reacted for two minutes whereafter it was washed off. The other was mixed with 100 mL of 0,5 molar HCl and reacted for 15 minutes until the mixture did not react anymore if more HCl was added. These samples were both dried overnight in a paper filter at room temperature and analysed under a microscope. With this method, the CaCO3-mud additive was still present in both samples, thus a higher concentration of HCl was chosen in the next method.
This method consisted of adding approximately 40 mL of 1 molar HCl until the sample was fully submerged. This mixture was then sat aside and let react out (approximately 10 minutes). Each sample was stirred three times in different phases of the reaction to ensure that all the material reacted. When no bubbles appeared at the top of the mixture anymore, indicating that it was done reacting, demi water was added to the sample to neutralize the sample. The mixture was then poured in a paper filter over a funnel and further washed with down demi water. The filter was marked with the sample number to prevent mix-up of the samples. When the water had passed through the filter, the wet sample was transferred to a 54-mu sieve. In this sieve, the sample was washed again, and fine clay particles were sieved out. Afterwards, the samples dried in the paper filters overnight at room temperature, either laid out on a flat surface with the container with the sample number next to it or in the numbered container. The process of the acidification of the samples and the drying of the samples is shown in Figure 18 and 19, respectively.

Figure 19: Acidification of the samples.

Figure 18: Drying process of the samples.

3.2 Gamma Ray

Each sample was measured with a GS-512i Portable Gamma Ray Spectrometer to determine which samples are potential clays. First, the GR device is tested by performing a background measurement 4 times without a sample on the table. This same measurement is then done at the same spot without a sample on a lead plate to determine if this lead plate can minimize background radiation.
The equipment is then tested to determine whether approximately 30 grams is enough to be able to differentiate the signal. For this test, three sands are selected with a varying GR signal from the well logs. Samples 1686, 1684 and 1679 are selected as light grey, very fine sands with a relatively low GR value. Samples 906, 905 and 907 are light-dark grey, coarse-grained sands with an average GR value. Finally, dark grey, coarse-grained, clayey sands are represented by samples 871, 870 and 869, with a relatively high GR value. The GR measurements of these samples were done 4 times each, the average was taken, and the measurements were plotted in a boxplot to display the spatial variability. These values are then compared to the relative ratios of the GR logs from the well-log report to conclude if these measurements can be used.

3.3 Infrared Spectroscopy

The FieldSpec 4 Hi-Res NG Spectroradiometer Analytical Spectral Device (ASD) is then used to measure the infrared spectra of the samples in the Delft Sandstone Region (2735- 2867 m MD). The device is first calibrated with a white reference to ensure reliable measurements. Beforehand, one sample is measured several times and mixed in between measurements to ensure that the spectrum of the sample is consistent throughout. Ten measurements of each sample are taken. The handheld device is cleaned between each sample to prevent cross-contamination.
This data is then loaded into the Spectragryph software. The ten measurements of each sample are averaged. The spectra are compared and grouped according to similarity and lithographic descriptions from the well logs. The characteristic peaks are identified and compared to a reference spectra library on spectral similarity. These results are then further analysed and compared to the literature.

4 Results

4.1 Gamma Ray Spectroscopy

The measurements of the GR spectrometer were plotted in a box plot. The TC, U, K and Th were plotted separately. First, the background measurements were plotted (Figure 20). There is a significant variance in measurements done without a lead plate. When placing a lead plate under the device, the variance of K and Th measurements is approximately 10% and the TC values 5% of the measurements without the lead plate (Table 3) Therefore, to minimize background radiation the lead plate was used for all sample measurements.

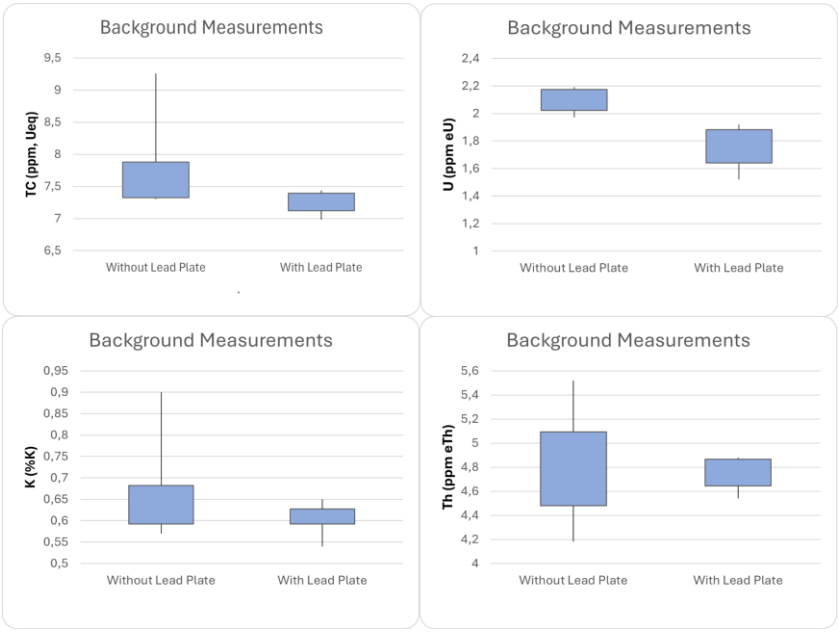

Figure 20: Boxplots of the TC, K, U and Th content of the background measurements.

Measurement	TC	K	U	Th
Variance without a lead plate	0,9	0,02	0,01	0,3
Variance with a lead plate	0,04	0,002	0,03	0,03

Table 3: Variance of the TC, K, U and Th content of the background measurements.

Next, the three distinct kinds of sand were plotted (Figure 21). In these plots, the variability differs per sample. The variability is inconsistent throughout the measurements done on one sample's TC, K, U and Th values (Table 4). No trend in the variance can be observed throughout the different samples or between the TC, K, U and Th values.

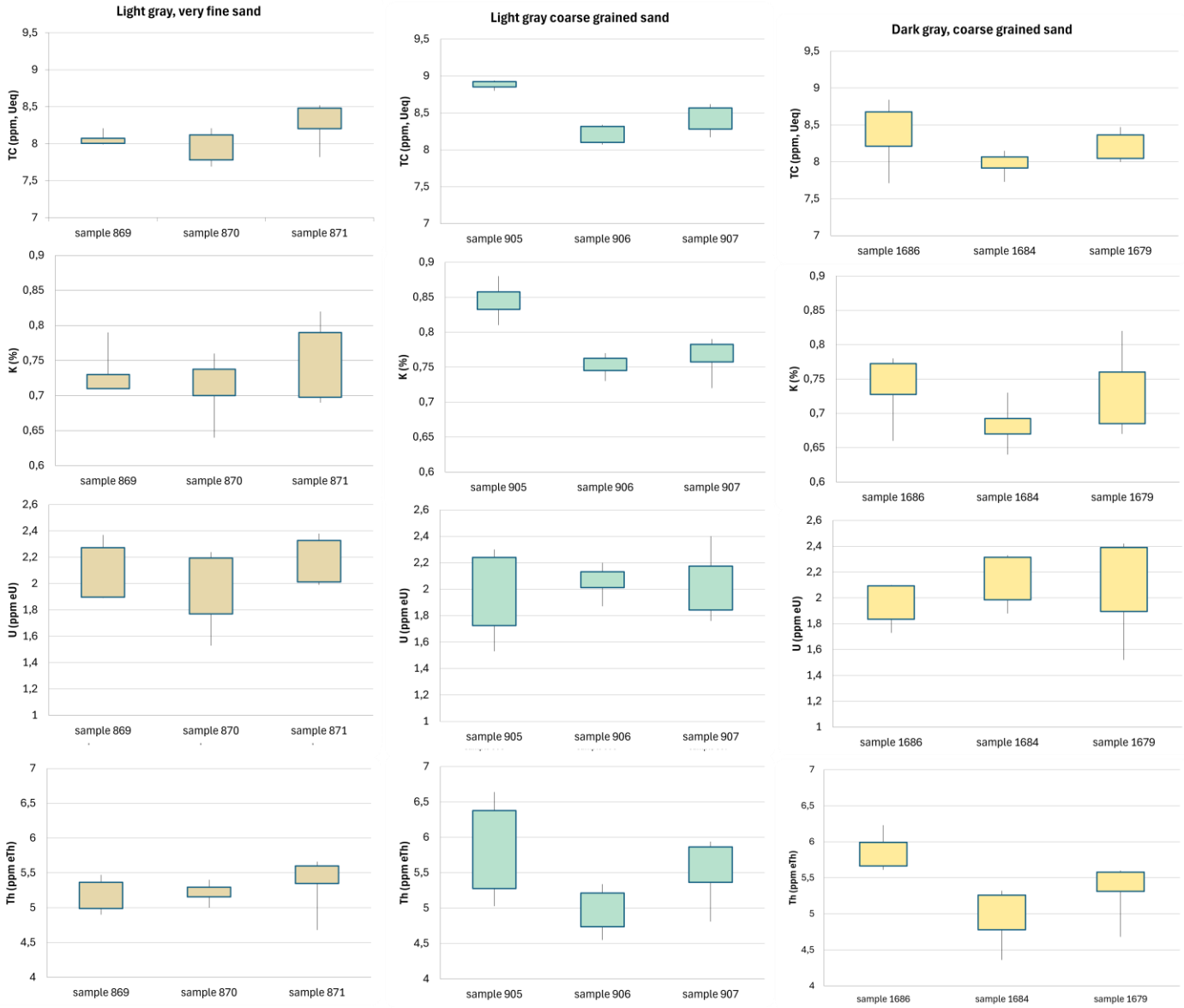

Figure 21: Boxplots of the TC, K, U and Th content of the different samples.

Sample	869	870	871	905	906	907	1679	1684	1686	Range
Var TC	0,008	0,058	0,103	0,004	0,137	0,043	0,049	0,032	0,239	**98,33%**
Var K	0,001	0,003	0,004	0,001	0,017	0,001	0,004	0,001	0,003	**75,00%**
Var U	0,044	0,108	0,413	0,132	0,139	0,080	0,174	0,049	0,032	**92,25%**
Var Th	0,053	0,027	0,215	0,576	0,357	0,261	0,196	0,190	0,078	**95,31%**

Table 4: Variance of the TC, K, U and Th content of the different samples.

Finally, the averages of the different samples were taken and plotted based on the sand type (Figure 22). It can be observed that the measurements without a lead plate give lower values than the measurements with a sample or with a lead plate. The measurements without lead plate give the highest average values. Furthermore, a trend can be seen throughout the samples between the different values of TC, K and Th. The measurements of U give a slightly different trend. The average values of the different samples have a range of 10 to 20% between the highest and the lowest values.

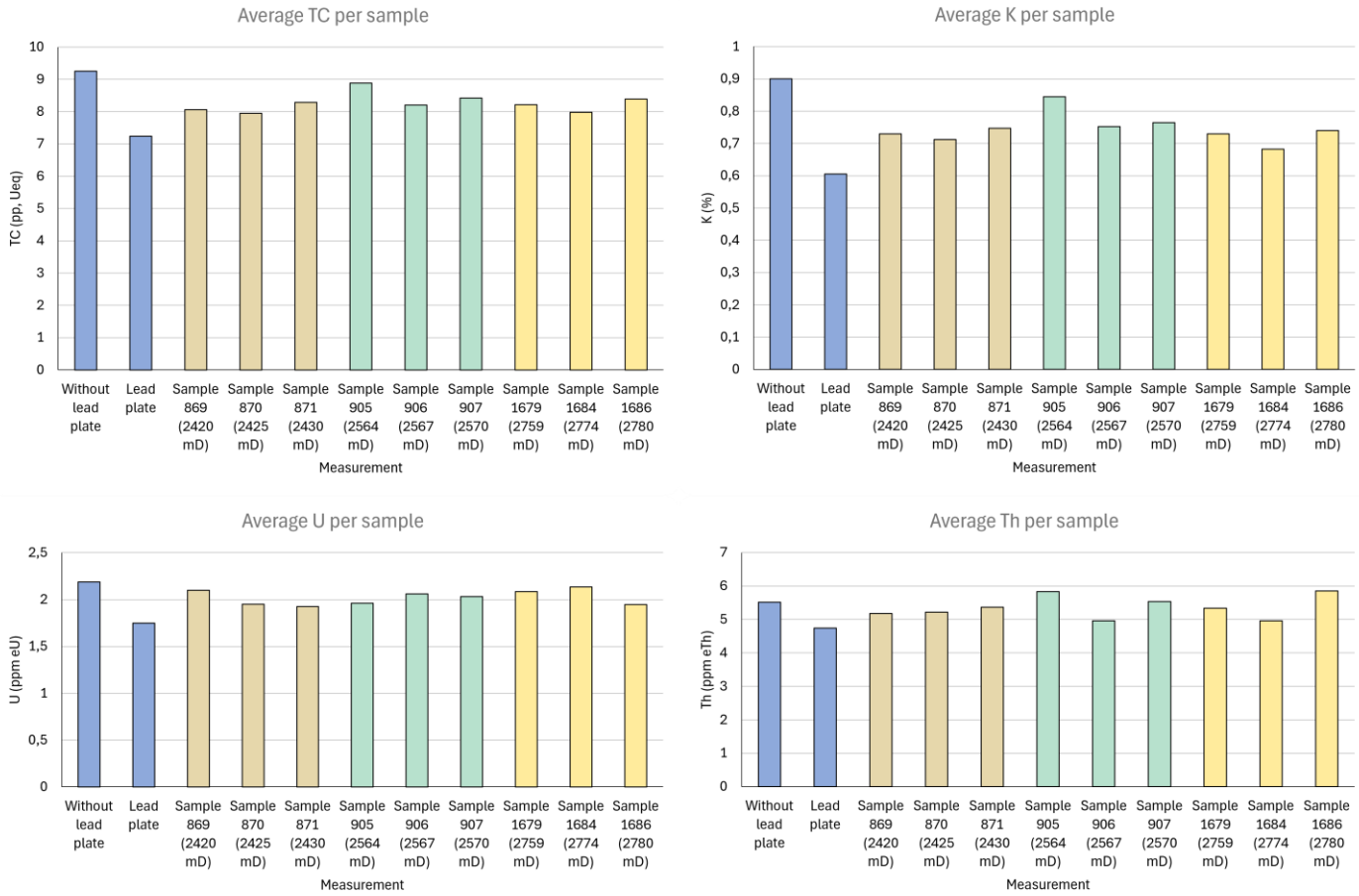

Figure 22: Averages of the TC, K, U and Th content of the different samples and background measurements.

	No sample
	Light gray, very fine sands
	Light-dark gray, coarse grained
	Dark gray, coarse grained, clayey

4.2 Infrared Spectroscopy

The measurements done with the ASD were plotted in Spectragryph v1.2.16.1 software. The average of the 10 measurements was taken and given the name of the corresponding sample number.
The different spectra were then divided into six groups based on depth, the wavelength of the peaks, shape, and the Spectrograph software classification. First, the peak positions were downloaded from the Spectragryph software (Table 5). These were sorted and divided into four groups. One that had no features at high wavelengths (I), one that had a peak around 1725 nm (IV and V), one that had peaks around 1315 nm (VI) and one that did not display any of these features (II and III). The spectra of these groups were plotted, and the spectra shapes were compared. Based on the difference in shape of the top of the 2100 nm feature groups II, III, IV and V were formed. Finally, these groups were compared to the top match of the classification done by the Spectragryph software (Appendix 3). In most cases, the spectra corresponded.

The peak positions of the different samples and the groups are shown in Table 5. The spectra of the different groups defined are shown in Figure 23 to 28. The spectra shapes are shown on the left (a) and the stacked spectra with peak positions are shown on the right (b).
Finally, the distinct features of each group are summarized in Table 6.

Depth	Sample number	Group	Wavelengths of the peak positions [nm]							
2735	1582	I	354	1413	1914	2207				
2738	1583	I	356	1413	1911	2207				
2741	1584	I	352	1413	1912	2207				
2744	1585	III	356	1413	1912	2207	2497			
2747	1586									
2750	1587	VI	1320	1413	1918	2207	2309	2496		
2753	1588	VI	352	1319	1413	1726	1918	2207	2309	2309
2756	1589	VI	352	1314	1413	1917	2207	2309	2492	
2759	1679	IV	352	1413	1725	1917	2207	2309	2461	
2765	1681	V	353	1413	1725	1912	2207	2310	2460	
2768	1682	III	352	1413	1916	2207	2497			
2771	1683	IV	1413	1725	1918	2207	2309	2460		
2774	1684	IV	353	1413	1725	1918	2207	2309	2460	
2777	1685	III	1413	1918	2207	2309				
2780	1686	III	1413	1916	2207	2310	2496			
2783	1687	II	357	1413	1918	2208	2309	2499		
2795	1691	III	353	1413	1913	2207	2350			
2798	1692	III	354	1413	1912	2207	2499			
2801	1693	V	354	1413	1724	1912	2207	2347		
2804	1694	V	356	1413	1725	1911	2207	2497		
2807	1695	I	354	1413	1910	2207				
2810	1696	I	1413	1910	2207	2499				
2816	1590	V	352	1413	1725	1913	2207			
2819	1591									
2822	1592	III	1413	1913	2207	2497				
2825	1593	VI	1315	1413	1915	2207	2310	2498		
2828	1594	III	1413	1913	2207	2309	2495			
2831	1595	VI	1090	1413	1725	1913	2207	2310	2461	
2834	1596	IV	1413	1725	1912	2207	2310	2465		
2837	1597	IV	1413	1725	1915	2207	2309	2460		
2840	1598	III	352	1413	1917	2207	2309	2492		
2843	1599	III	353	1413	1913	2207	2350	2496		
2846	1698	II	1413	1918	2207	2309	2497			
2849	1699	I	353	1413	1913	2207				
2855	1700	I	354	1413	1913	2207				
2864	1702	IV	353	1413	1724	1918	2207	2309		
2867	1703	IV	1413	1725	1916	2207	2309	2465		

Table 5: Overview of depth, sample number, group, and wavelengths of the peak positions.

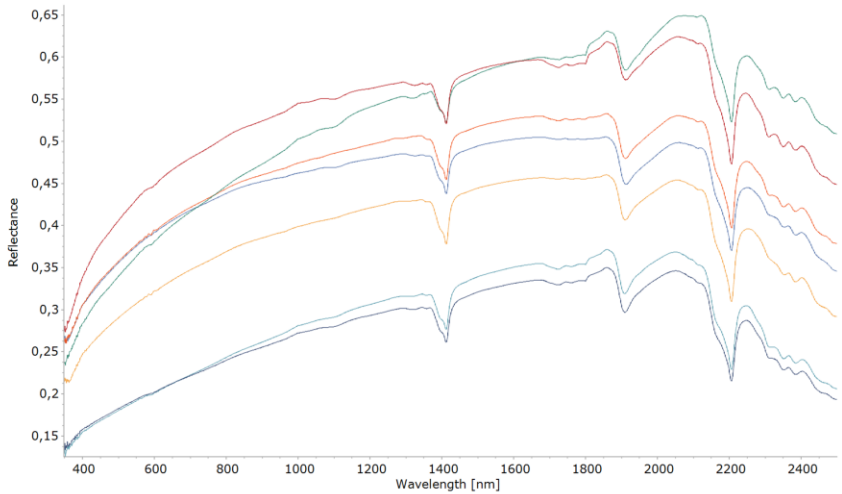

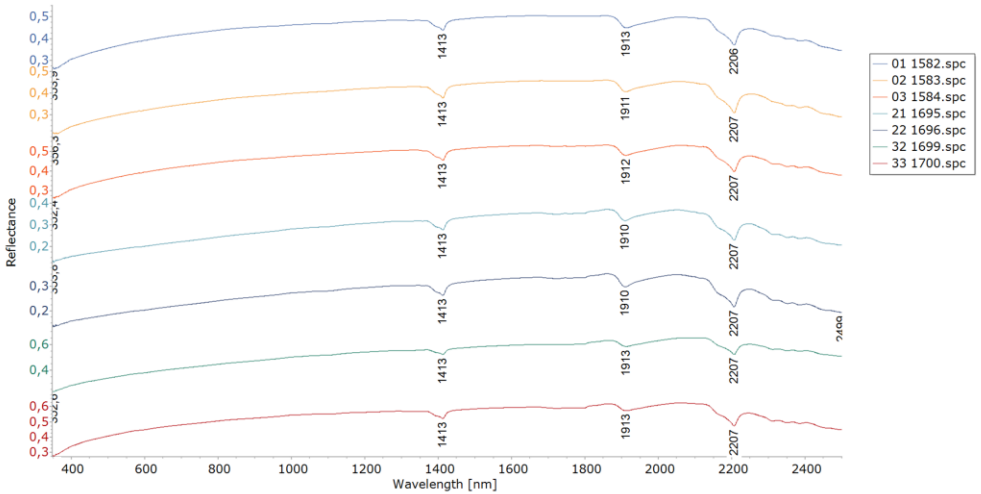

Figure 23: Group I a) spectrum shapes **b) stacked spectra with peak positions.**

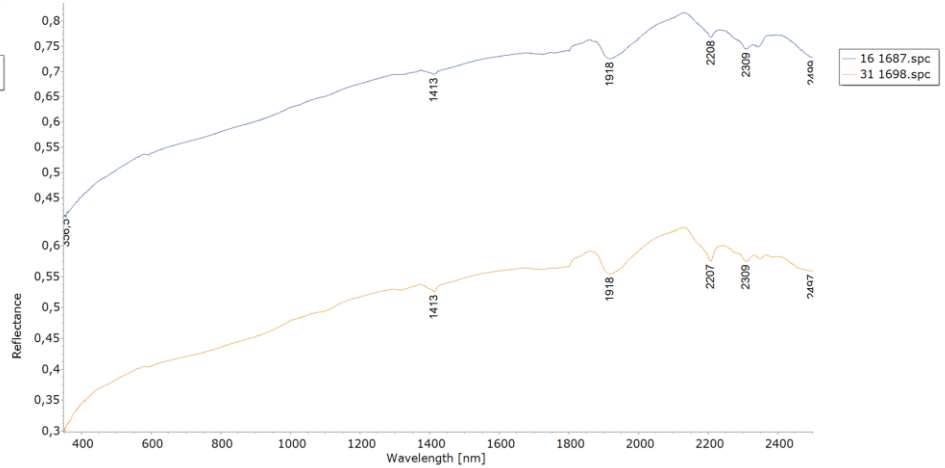

Figure 24: Group II a) spectrum shapes **b) stacked spectra with peak positions.**

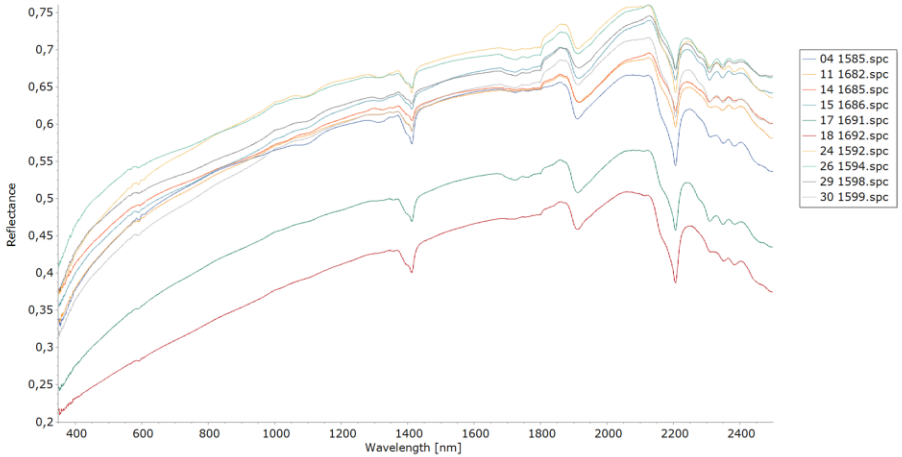

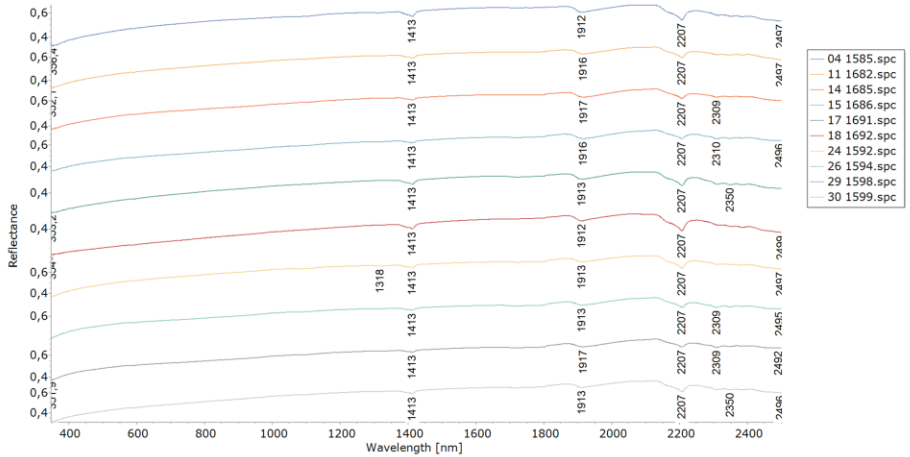

Figure 25: Group III a) spectrum shapes **b) stacked spectra with peak positions.**

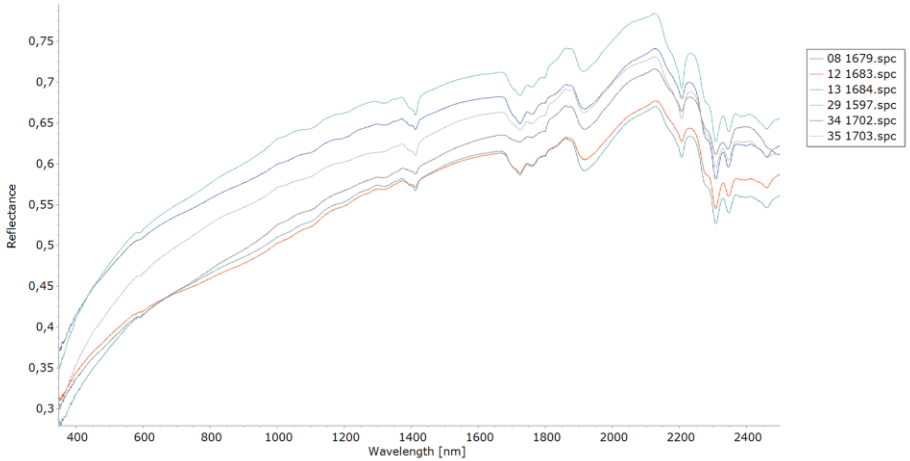

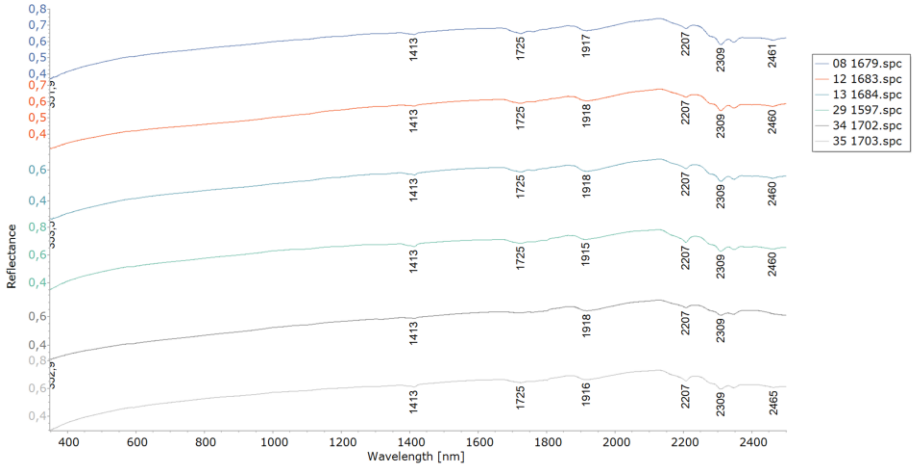

Figure 26: Group IV a) spectrum shapes **b) stacked spectra with peak positions.**

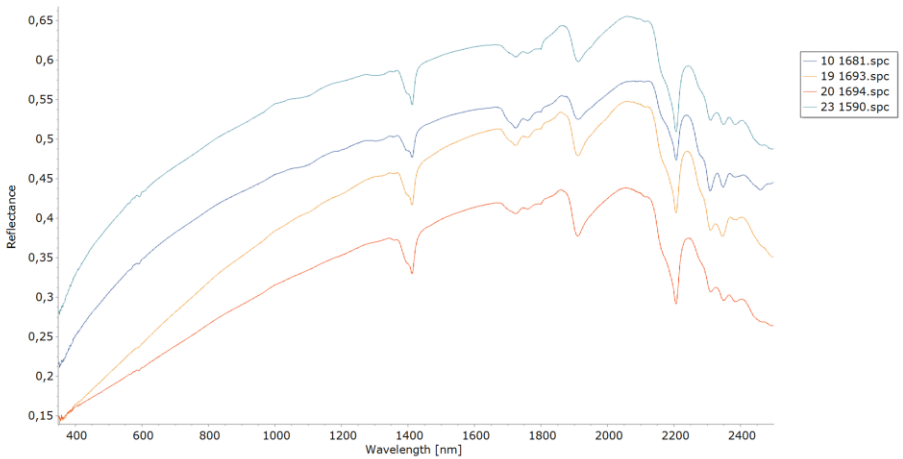

Figure 27: Group V a) spectrum shapes

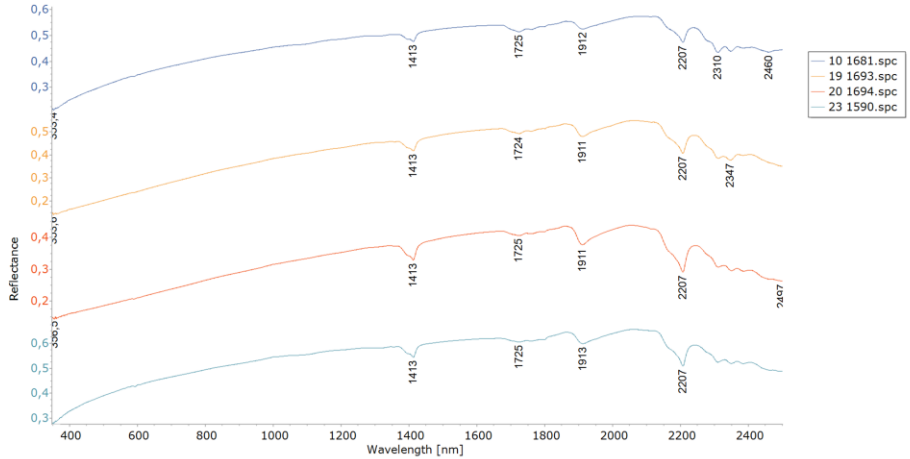

b) stacked spectra with peak positions.

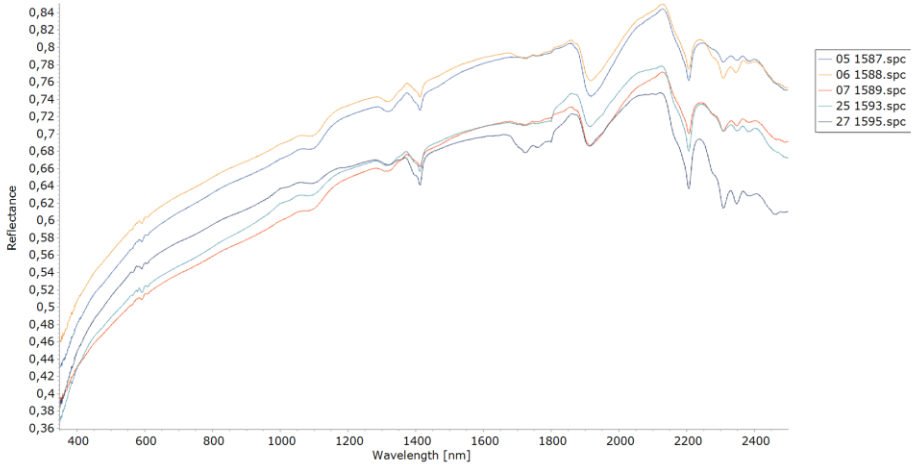

Figure 28: Group VI a) spectrum shapes

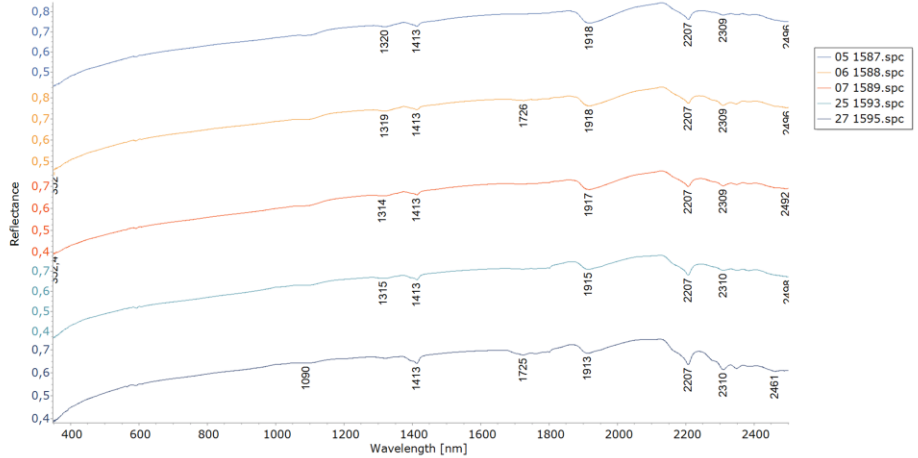

b) stacked spectra with peak positions

Group	Sample numbers	Distinct features
I	1696 1584 1699 1695 1700 1582 1583	Clear peak positions at 1413, 1913, and 2206 Slight double peak at 1400 and 1413 nm (double OH absorption) Similar shape Triple feature between 2200 and 2400 nm
II	1698 1687	Distinct shape of the spectrum that does not match the others. Single OH absorption at 1413 nm. Shallow 1400 feature
III	1598 1594 1686 1599 1682 1592 1585 1692 1685 1691	Peak positions at 1413, 1915, 2207, 2497 Single OH absorption at 1413. Flat top of the spectrum from 2050 to 2122 nm
IV	1683 1684 1597 1679 1703 1596 1702	Peak positions at 1413, 1725, 1915, 2207, 2309, 2460 Sharper top shape of 2100 nm top when compared to category V. Single OH absorption at 1413
V	1681 1694 1693 1590	Peak positions at 1413, 1725, 1912, 2207 Peaks around 1700 nm Flat shape of 2100 nm top when compared to category IV. Single OH absorption
VI	1595 1589 1587 1593 1588	Distinct peak at 1300 nm Single OH absorption

Table 6: Distinct features of the different spectrum groups.

5 Discussion

5.1 Gamma Ray

The Gamma Ray measurements were done to attempt to corelate the handheld measurements to the GR log values obtained during drilling and identify the depth of clay phases.

When looking at the averaged Gamma Ray plots (Figures 29 and 30), it can be observed that the different samples have a 10 to 20% range between the minimum and maximum measurements of the TC, K, U and Th values (Table 7). The overall average is consistent throughout the samples. In the GR log values from the well logs for sample 905, 906, 907, 1679, 1684 and 1686 (Appendix 4) (Baker Hughes, 2023) a relatively high range of 81% between the different depths that correlate to the samples (Figure 29, table 7). For sample 869, 870 and 871 no well log data was available. The TC range of the samples is 10%. From this, the conclusion can be drawn that the GR values from the logs cannot be correlated to the GR values measured by the GR spectrometer. This is probably due to the small sample size since the tool is manufactured for use in the field on larger rock bodies (SatisGeo, 2015).

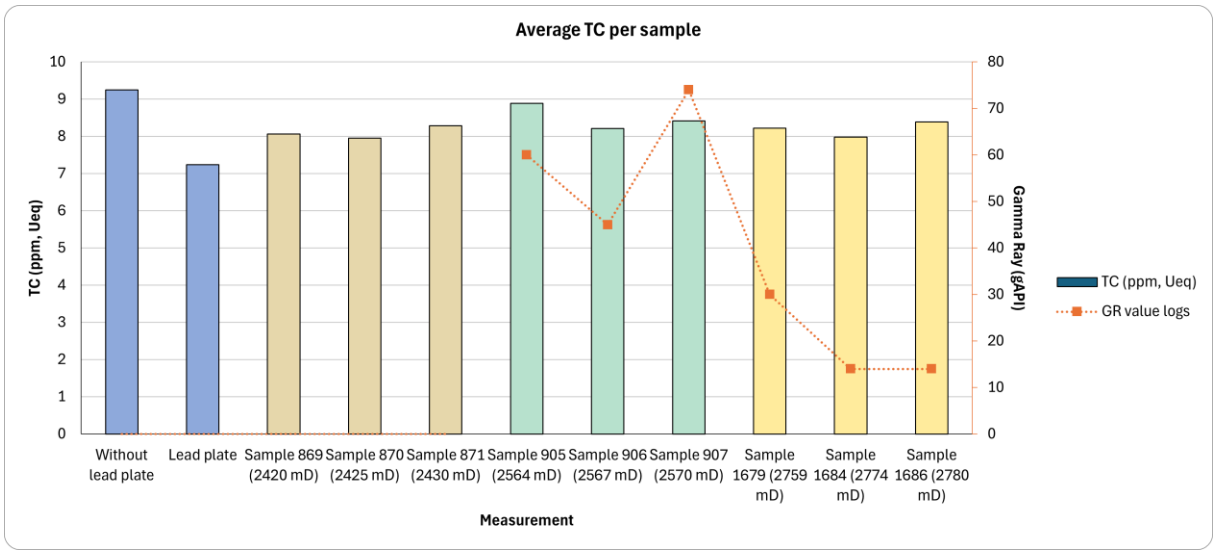

Figure 29: Average of 4 measurements taken per sample TC and GR values for well logs.

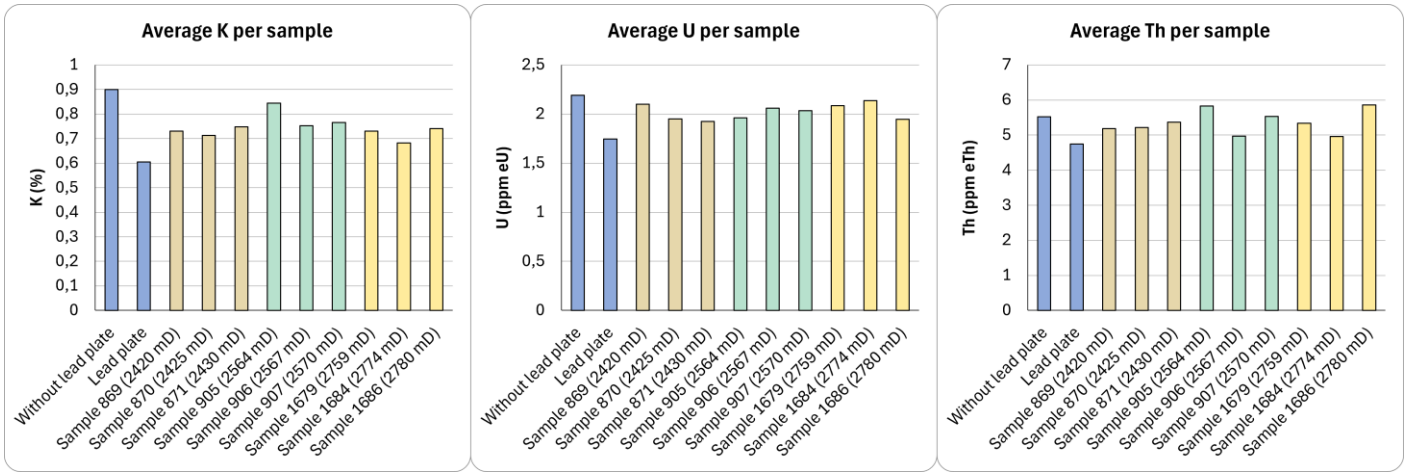

Figure 30: Average of 4 measurements taken per sample of K, U and Th.

Measurement	TC (ppm, Ueq)	K (%)	U (ppm eU)	Th (ppm eTh)	GR (gAPI)
Range in %	10%	19%	10%	15%	81 %

Table 7: Range of the averaged TC, K and Th measurements per sample and the GR log values.

When looking at the different boxplots for TC (figure 31, table 8), it can be observed that the variance between measurements differs per sample, while the conditions in which measurements are taken are the same. From this result, it is concluded that the device does not measure accurately enough to be able to differentiate between the samples.

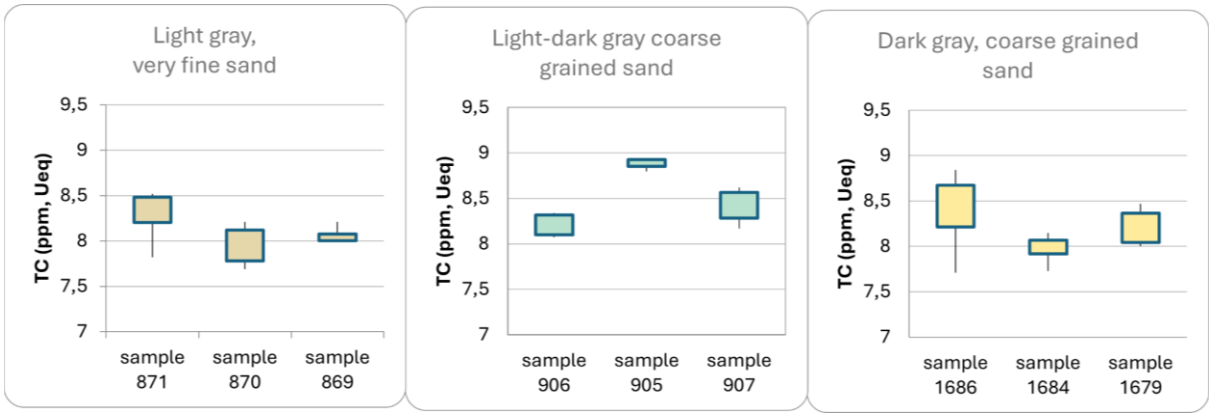

Figure 31: Boxplot of TC values of different sand samples.

Sample	**871**	**870**	**869**	**906**	**905**	**907**	**1686**	**1684**	**1679**
Variance	0,1	0,06	0,01	0,02	0,004	0,04	0,24	0,03	0,05

Table 8: Variance of the different measurements.

When comparing the GR logs to the NIR spectra interpretations no correlation can be seen between the mineral spectra and the GR log values. This can be explained by the fact that ASD only measures minerals present but does not the measure quantity of these minerals, which is measured by the Gamma Ray. Another possibility is that the depths of the GR logs and the given depth of the samples do not match up.

5.2 Infrared Spectroscopy

The Infrared Spectroscopy was done to identify the clay minerals in the samples that have the potential to contain lithium.
All the spectra were loaded into the Spectragryph Identify tool and were compared in the wavelength of 350-2500 nm to the library spectra *USGS_splib06_Minerals_881spectra* spectral database (Kokaly et al., 2017). The spectrum with the highest percentage match with one of the lithium-bearing library spectra from each group is chosen (Table 9). This spectrum is then compared to the library spectrum it matched with.

Group	Sample number	Top match	Percentage match
I	1583	Kaolinite_CM7_NIC4bb_RREF	97,58
II	1698	Chlorite_HS179.1B_ASDFRb_AREF Illite_IL105_(1Md)_BECKb_AREF	97,65 96,55
III	1692	Illite_GDS4.2_Marblehead_ASDNGb_AREF	99,1
IV	1703	Illite_IL105_(1Md)_BECKb_AREF	98,46
V	1693	Illite_GDS4.2_Marblehead_ASDNGb_AREF	98,44
VI	1588	Illite_IL105_(1Md)_BECKb_AREF	98,62

Table 9: Group, sample number, top match classification and percentage match.

These spectra were analysed by comparing the absorption positions to the sample spectra in Spectragryph and literature. All the samples in group I were defined as kaolinite by the Spectragryph software. The absorptions of spectra as well as the shape were compared to the library spectrum found in the literature as discussed in the background section. Kaolinite exhibits distinct absorptions at 1400, 1412, 1830, 2162, 2206, 2312, 2350, and 2380 nanometres (AusSpec International, 2008). The chosen sample spectrum (blue) and the library spectrum of kaolinite (pink) with matching peaks indicated are shown in Figure 32.

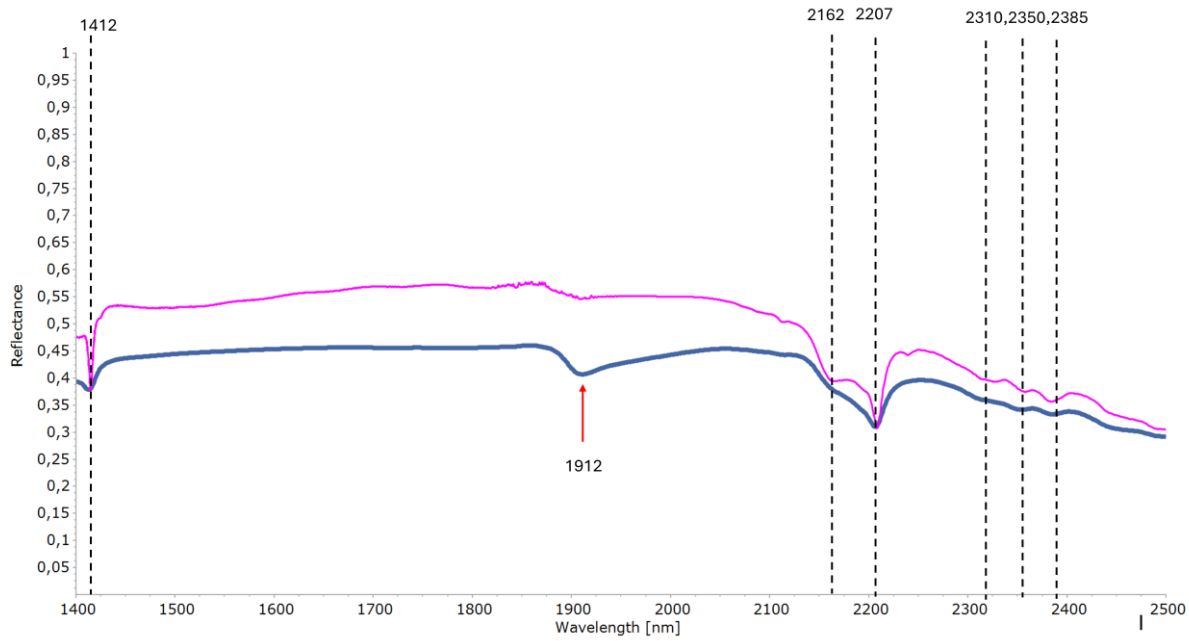

Figure 32: Group I spectrum 1583 (blue) and Kaolinite_CM7_NIC4bb_RREF (pink), with the absorptions indicated.

The slight dip at 2162 is very shallow, indicating low crystallinity. The absorption at 1912 nm indicated by the red arrow indicates that the sample is slightly hydrated (AusSpec International, 2008). The characteristic 3 absorptions of kaolinite at the end of the spectrum at 2312, 2350 and 2380 nm can be distinguished. (AusSpec International, 2008).

Groups III, IV, V and VI are all characterized as illite by the Spectragryph software. Illite displays characteristic absorptions at 1410, 1912, 2180-2228, 2347 and 2440 nm (AusSpec International, 2008). These can be recognized in all 4 spectra indicated by the dotted lines (Figure 33-36). Illite can be recognized by the single sharp OH absorption around 1410 and a single sharp AlOH absorption that varies in wavelength from 2180-2228 nm depending on composition. The two absorptions 2347 and 2440 nm are known to persist in mixed spectra and can be used to identify illite (AusSpec International, 2008).

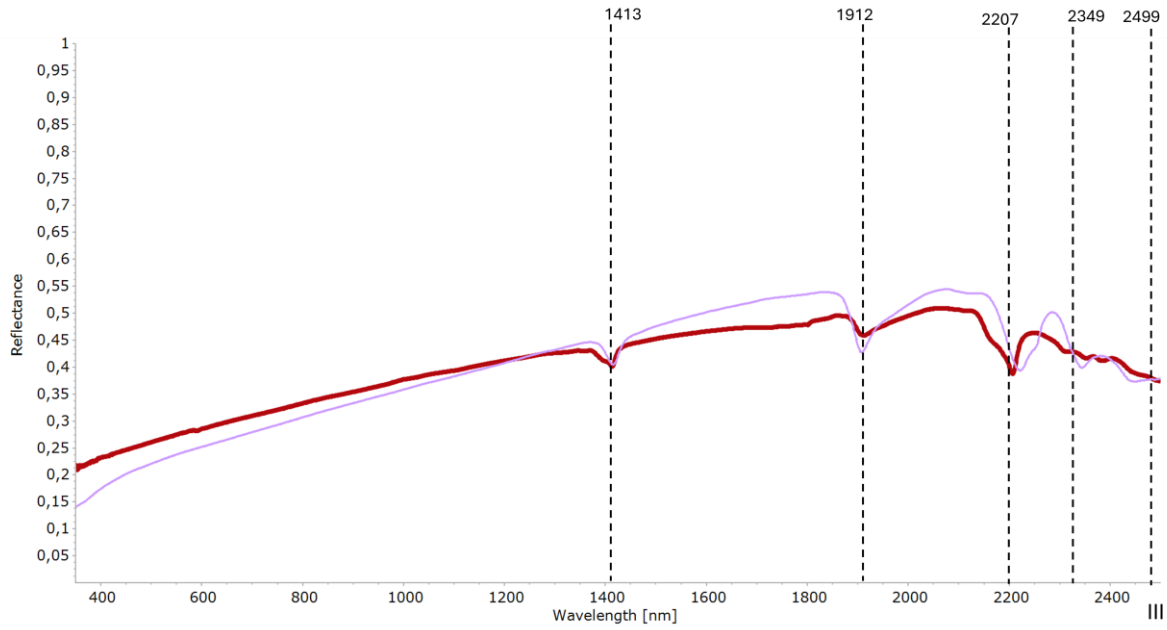

Figure 33: Group III spectrum 1692 (red) and Illite_GDS4.2_Marblehead_ASDNGb_AREF (purple), with the absorptions indicated.

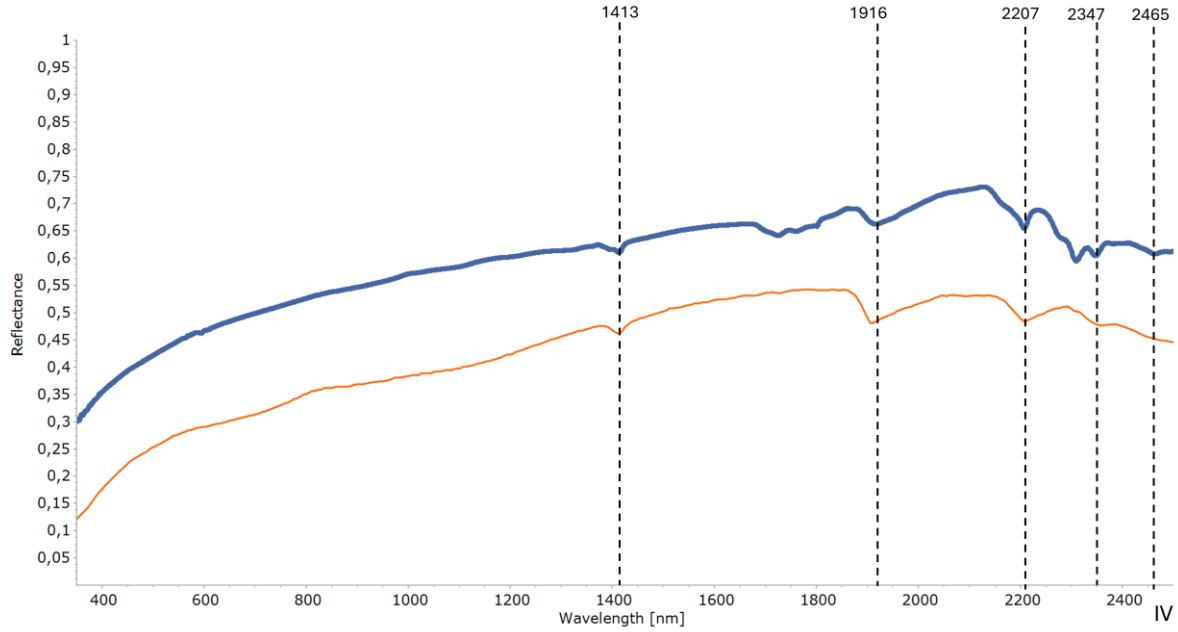

Figure 34: Group IV spectrum 1703 (blue) and Illite_IL105_(1Md)_BECKb_AREF (orange), with the absorptions indicated.

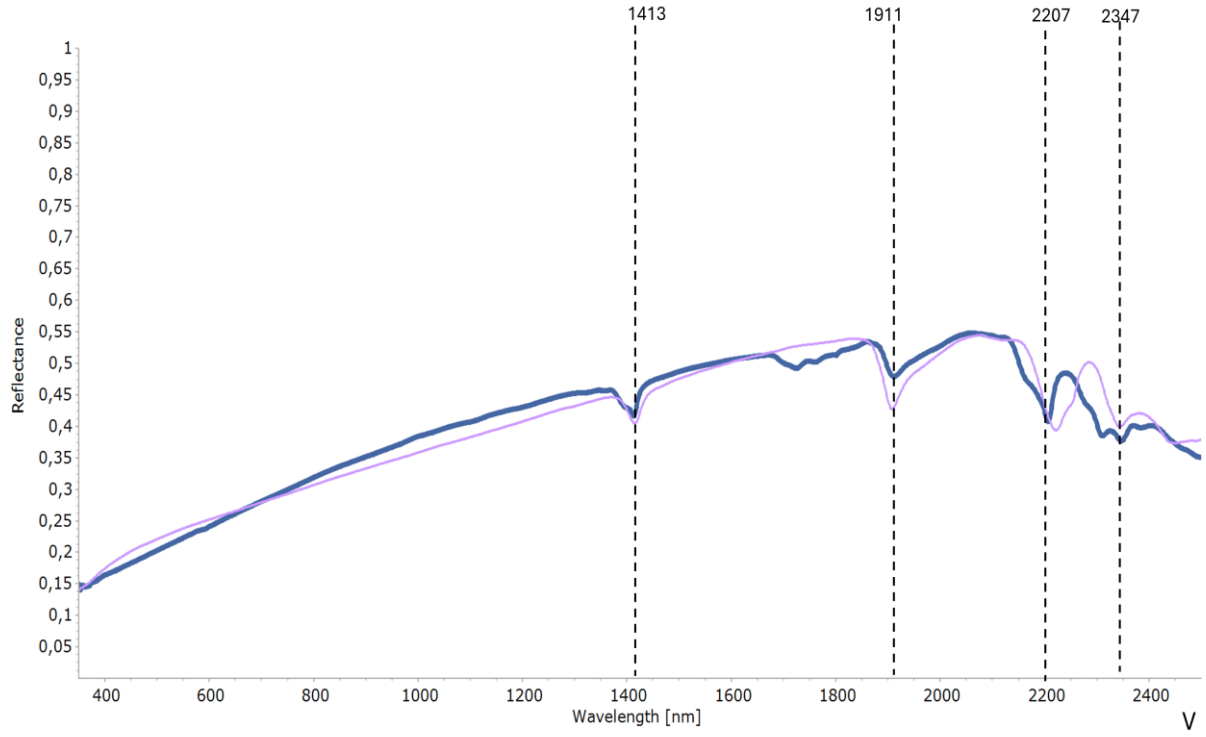

Figure 35: Group V spectrum 1693 (blue) and Illite_GDS4.2_Marblehead_ASDNGb_AREF (purple) with the absorptions indicated.

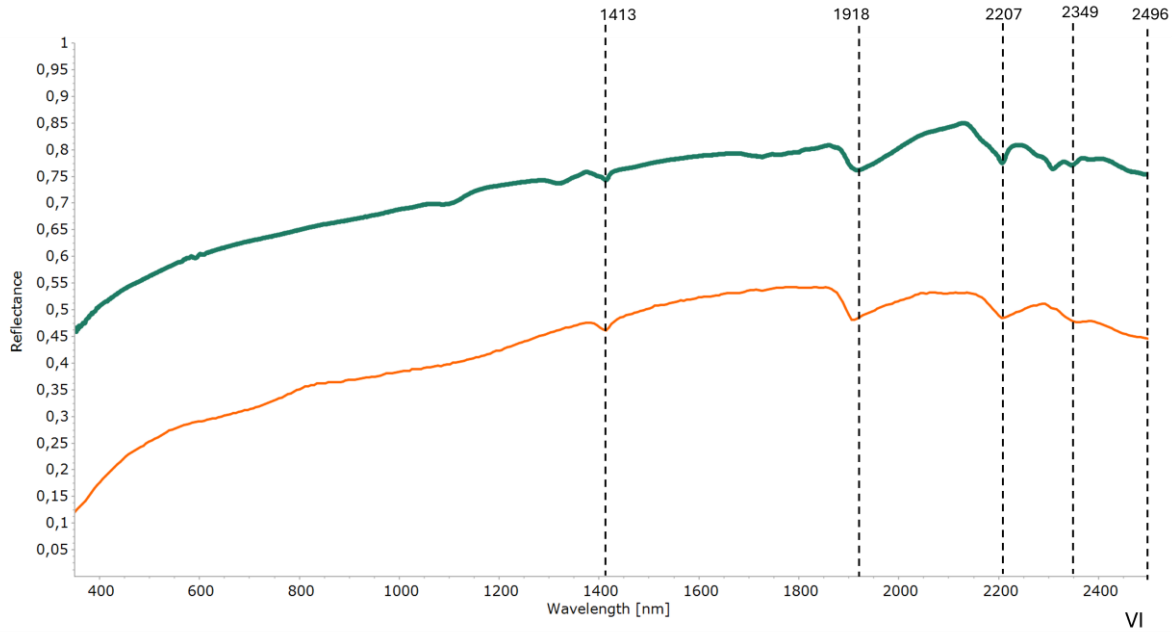

Figure 36: Group VI spectrum 1588 (green) and Illite_IL105_(1Md)_BECKb_AREF (orange), with the absorptions indicated.

When comparing these 4 spectra a difference in the intensity of the absorption throughout the spectrum can be observed. The absorption at 1912 nm can be seen in all four spectra. This feature indicates water absorption. If this feature is sharper, this can indicate increasing crystallinity (AusSpec International, 2008). The difference in intensity of the absorptions can

also be due to the difference in grain size between the samples. Smaller grains increase reflectance scatter, which reduces the absorption peak height (Waiser et al., 2007).

Sample 1703 and 1588 (Figure 34 and 36) are matched with a different library spectrum of illite than sample 1692 and 1693 (Figure 33 and 35). When looking at the description of the grain size in the well report of these samples, sample 1703 and 1588 (Figure 34 and 36) have medium to fine grains. Sample 1692 and 1693 (Figure 33 and 35) are described to consist of medium to coarse grains (Geothermie Delft, 2023). This coarser grain size can be seen by more defined peaks throughout the spectrum (Figure 2 and 4).

For group II (Figure 37) both samples were identified as chlorite when using the Spectragryph Identify tool. Chlorite has characteristic absorption at 750, 928, 1130, 2340-2256 and 2330-2360 nm (AusSpec International, 2008). However, when looking at the shape of the spectra as well as the absorption positions it matches illite (orange) better. When comparing the absorption positions of chlorite (green) do not align with the absorptions of the sample spectrum. When comparing the sample to the illite library spectrum a clear match of the absorption positions as well as peak shape are sheen. Therefore, this group is classified as illite.

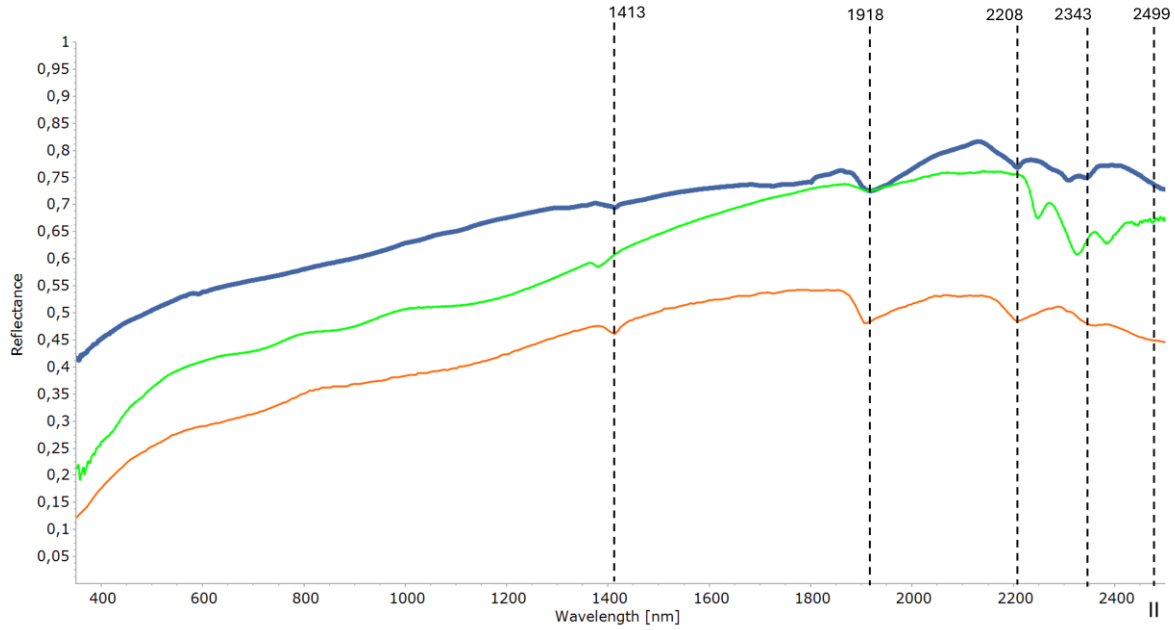

Figure 37: Group II spectrum 1698 (blue) compared to Chlorite_HS179.1B_ASDFRb_AREF (yellow) and Illite_IL105_(1Md)_BECKb_AREF (green), with the absorptions indicated.

6 Conclusion

To conclude, in this thesis, the feasibility of extracting lithium from the DAP well is discussed. The spatial variabilities of potential sources for Lithium in the Delft sandstone reservoir were determined. Potential clay minerals that are likely to be found within the Delft Sandstone layer are kaolinite and illite. The spectra of different samples taken during the drilling of the DEL-GT-01 well display features of these two minerals. These minerals could potentially contain lithium if metals in the molecular structure of these clays were replaced with Li+ during formation or weathering. This is most likely to occur in volcanic regions, which have not been present in the Netherlands for a long time. However, the transport of volcanic sediment could have occurred, resulting in lithium-rich clay. Further research must be done on the molecular structure elemental analysis of this potential kaolinite and illite. As no minerals are present that contain lithium in their regular molecular structure this is not very feasible. Therefore, it was concluded that there could be potential for lithium-bearing clay in the Delft Sandstone in kaolinite or illite clays, but further research must be done to confirm lithium in their structure.

The gamma-ray device was concluded not to be able to differentiate between small quantity samples. Consequently, a comparison with the GR well logs was not possible. When comparing the ASD analysis to the well logs no correlation was found as the ASD did not measure the quantity of the minerals present. As only the well logs were available and not the data values, a comparison of the K value per sample could not be done. It can be concluded that it is not possible to use handheld gamma-ray measurements on samples of rock cuttings can provide overall trends similar to the more expensive high-resolution well-logs in this case.

7 Future outlook

When looking at the future, there is certainly potential to extract lithium from geothermal wells. However, presently there are no economically feasible methods to extract this lithium from clays. As for the DAP well, more research has to be done on the molecular structure of the clay minerals present. The minerals found that can potentially contain lithium are kaolinite and illite. The chance of there being lithium in these minerals in the Delft Sandstone layer is not high as the depositional environment is not right. Furthermore, there are no minerals that have naturally occurring lithium in their molecular structure present to leach lithium into other clays.

Further research steps for this research are using different equipment that can measure Gamma Ray in samples. These values can be related to the Gamma Ray logs to correlate the depths of the samples to the depths of the well logs. The measurements per sample can give more clarity on the different minerals present by comparing the K values.
The next step for Infrared Spectroscopy could be an elemental analysis of the samples to determine if lithium is present in the mineral structure. Analysis of the place of the lithium in the molecular structure can be done to examine if the lithium can be extracted if present.

References

Arnold, D., Debertin, K., Heckel, A., Kanisch, G., Wershofen, H., Wilhelm, C., Physikalisch-Technische Bundesanstalt, Federal Office for Radiation Protection, Thünen Institute of Fisheries Ecology, & Karlsruhe Institute of Technology. (2018). Procedures Manual for monitoring of radioactive substances in the environment and of external radiation [Procedures Manual]. In Procedures Manual for monitoring of radioactive substances in the environment and of external radiation (March 2018). https://www.bmuv.de/fileadmin/Daten_BMU/Download_PDF/Strahlenschutz/Messanleitungen_2022/gamma_spekt_grundl_v2018-03_en_bf.pdf

AusSpec International. (2008). Spectral Interpretation Field Manual (3de editie). GMEX.

Baker Hughes. (2023). Magnetic Resonance Explorer Log GT-01 (File no: 207823).

Benson, T. R., Coble, M. A., & Dilles, J. H. (2023). Hydrothermal enrichment of lithium in intracaldera illite-bearing claystones. Science Advances, 9(35). https://doi.org/10.1126/sciadv.adh8183

Bronzino, J. D. (2012). Radiation imaging. In Elsevier eBooks (pp. 995–1038). https://doi.org/10.1016/b978-0-12-374979-6.00015-0

Büyükburç, A., Maraşlıoğlu, D., Bilici, U., & Köksal, G. (2006). Extraction of lithium from boron clays by using natural and waste materials and statistical modelling to achieve cost reduction. Minerals Engineering, 19(5), 515–517. https://doi.org/10.1016/j.mineng.2005.11.003

Cao, L., Xie, W., Cui, H., Xiong, Z., Tang, Y., Zhang, X., & Feng, Y. (2022). Fibrous Clays in Dermopharmaceutical and Cosmetic Applications: Traditional and Emerging Perspectives. International Journal Of Pharmaceutics, 625, 122097. https://doi.org/10.1016/j.ijpharm.2022.122097

Capon, A. (2021, June 24). Can lithium supply keep up with strong EV demand? Institutional Investor. Retrieved April 4, 2024, from https://www.institutionalinvestor.com/article/2bswqvt5gr58738z0fwu8/innovation/can-lithium-supply-keep-up-with-strong-ev-demand

Christmann, P., Gloaguen, É., Labbé, J., Melleton, J., & Piantone, P. (2015). Global Lithium Resources and Sustainability Issues. In Elsevier eBooks (pp. 1–40). https://doi.org/10.1016/b978-0-12-801417-2.00001-3

Classification and mineralization of global lithium deposits and lithium extraction technologies for exogenetic lithium deposits. (2023). ScienceDirect. https://doi.org/10.31035/cg2023061

Díaz-Curiel, J., Miguel, M. J., Biosca, B., & Díaz, M. I. (2021). Gamma ray log to estimate clay content in the layers of water boreholes. Journal Of Applied Geophysics, 195, 104481. https://doi.org/10.1016/j.jappgeo.2021.104481

Donselaar, M. E., Groenenberg, R., & Gilding, D. T. (2015). Reservoir Geology and Geothermal Potential of the Delft Sandstone Member in the West Netherlands Basin. ResearchGate. https://www.researchgate.net/publication/311100231_Reservoir_Geology_and_Geothermal_Potential_of_the_Delft_Sandstone_Member_in_the_West_Netherlands_Basin

Firestone, R. B. & Lawrence Berkeley National Laboratory. (2005). Physics of Gamma-ray Spectroscopy Measurements. In Workshop on Nuclear Data for Activation Analysis. https://indico.ictp.it/event/a04183/session/35/contribution/20/material/0/0.pdf

Geothermie Delft & Geo Service GMBH. (2023). Final Well Report Geothermie Delft DEL-GT-01.

Grant, A., Whittaker, M., & Celestian, A. (2020). Inside Tesla's lithium clay salt extraction process — Jade Cove Partners. Jade Cove Partners. Retrieved March 15, 2024, from https://www.jadecove.com/research/teslasaltclay

Gregory, A., & Horwood, J. L. (1961). A LABORATORY STUDY OF GAMMA-RAY SPECTRA AT THE SURFACE OF ROCKS. https://doi.org/10.2172/4833372
Grunenwald, A., Keyser, C., Sautereau, A., Crubézy, É., Ludes, B., & Drouet, C. (2014). Revisiting carbonate quantification in apatite (bio)minerals: a validated FTIR methodology.
Halliburton. (2023). Daily Drilling Fluid Report DEL-GT-01 2023-09-19 (Report No: 072).
Journal Of Archaeological Science, 49, 134–141. https://doi.org/10.1016/j.jas.2014.05.004
Judit Tóth, Udvardi, Kovács, Loránd, Falus, Szabó, Troskot-Čorbić. (2010). Analytical development in FTIR analysis of clay minerals. Mol Group Scienticic Magazine. https://mol.hu/images/pdf/A_MOL_rol/Mediaszoba/MOL_Group_Szakmai_Tudomanyos_Kozlemenyek/SZTK_2012-1-1.pdf#page=52
Kaufhold, S., Hein, M., Dohrmann, R., & Ufer, K. (2012). Quantification of the mineralogical composition of clays using FTIR spectroscopy. Vibrational Spectroscopy, 59, 29–39. https://doi.org/10.1016/j.vibspec.2011.12.012
Kavanagh, L., Keohane, J., Garcia-Cabellos, G., Lloyd, A., & Cleary, J. (2018). Global Lithium Sources—Industrial Use and Future in the Electric Vehicle Industry: A review. Resources (Basel), 7(3), 57. https://doi.org/10.3390/resources7030057
Killeen, P. G., Mwenifumbo, C. J., & Ford, K. L. (2015). Tools and Techniques: Radiometric Methods. In Elsevier eBooks (pp. 447–524). https://doi.org/10.1016/b978-0-444-53802-4.00209-8
Król-Morkisz, K., & Pielichowska, K. (2019). Thermal decomposition of polymer nanocomposites with functionalized nanoparticles. In Elsevier eBooks (pp. 405–435). https://doi.org/10.1016/b978-0-12-814064-2.00013-5
Laukamp, C., Rodger, A., LeGras, M., Lampinen, H., Lau, I., Pejcic, B., Stromberg, J., Francis, N., & Ramanaïdou, E. (2021). Mineral Physicochemistry Underlying Feature-Based Extraction of Mineral Abundance and Composition from Shortwave, Mid and Thermal Infrared Reflectance Spectra. Minerals, 11(4), 347. https://doi.org/10.3390/min11040347
Li, H., Eksteen, J., & Kuang, G. (2019). Recovery of lithium from mineral resources: State-of-the-art and perspectives – A review. Hydrometallurgy, 189, 105129. https://doi.org/10.1016/j.hydromet.2019.105129
Madejová, J., Gates, W. P., & Petit, S. (2017). IR Spectra of Clay Minerals. In Developments in Clay Science (pp. 107–149). https://doi.org/10.1016/b978-0-08-100355-8.00005-9
Malvern Panalytical. (z.d.). ASD FieldSpec | Field Portable Spectroradiometers. https://www.malvernpanalytical.com/en/products/product-range/asd-range/fieldspec-range?utm_source=google&utm_medium=cpc&utm_campaign=EN%20-%20WESEU%20-%20Search&utm_term=fieldspec4&utm_content=EN%20-%20Product%20-%20Aeris%20Range&gad_source=1&gclid=Cj0KCQjw5cOwBhCiARIsAJ5njuYUMQVece8aXCrWjsDgwid6hpGorsU1TOqD2rRhr2_-TE74z_StUGsaArISEALw_wcB
Martin, G., Rentsch, L., Höck, M., & Bertau, M. (2017). Lithium market research – global supply, future demand and price development. Energy Storage Materials, 6, 171–179. https://doi.org/10.1016/j.ensm.2016.11.004
Mason, B. H., (1958), Principles of geochemistry (2d ed): New York, John Wiley, 329 p
McCay, A. T., Harley, T. L., Younger, P., Sanderson, D., & Cresswell, A. (2014b). Gamma-ray Spectrometry in Geothermal Exploration: State of the Art Techniques. Energies, 7(8), 4757–4780. https://doi.org/10.3390/en7084757
Kokaly, R.F., Clark, R.N., Swayze, G.A., Livo, K.E., Hoefen, T.M., Pearson, N.C., Wise, R.A., Benzel, W.M., Lowers, H.A., Driscoll, R.L., and Klein, A.J., 2017, USGS Spectral Library Version 7: U.S. Geological Survey Data Series 1035, 61 p., https://doi.org/10.3133/ds1035.
Millot, Georges, (1970), Geology of clays; weathering, sedimentology, and geochemistry: New York, Springer-Verlag, 429 p
Newman, A.C.D. and G. Brown (1987) The chemical constitution of clays. In Newman, A.C.D. (Ed) Chemistry of Clays and Clay Minerals. Mineralogical Society Monograph No.6. John Wiley and Sons, New York NY: 1-128

Nurhandoko, B. E. B., Kurniadi, R., Hadi, M. R. A., & Komara, I. R. (2017). Study of gamma spectrometry laboratory measurement in various sediment and vulcanic rocks. Journal Of Physics: Conference Series, 799, 012027. https://doi.org/10.1088/1742-6596/799/1/012027
Peiró, L. T., Villalba, G., & Ayres, R. U. (2013). Lithium: Sources, production, uses, and recovery outlook. JOM (1989), 65(8), 986–996. https://doi.org/10.1007/s11837-013-0666-4
Physikalisch-Technische Bundesanstalt, Federal Office for Radiation Protection, Thünen Institute of Fisheries Ecology, & Karlsruhe Institute of Technology. (2018). Procedures Manual for monitoring of radioactive substances in the environment and of external radiation [Procedures Manual]. In Procedures Manual for monitoring of radioactive substances in the environment and of external radiation (March 2018). https://www.bmuv.de/fileadmin/Daten_BMU/Download_PDF/Strahlenschutz/Messanleitungen_2022/gamma_spekt_grundl_v2018-03_en_bf.pdf
Procedures Manual for monitoring of radioactive substances in the environment and of external radiation [Procedures Manual]. In Procedures Manual for monitoring of radioactive substances in the environment and of external radiation (March 2018). https://www.bmuv.de/fileadmin/Daten_BMU/Download_PDF/Strahlenschutz/Messanleitungen_2022/gamma_spekt_grundl_v2018-03_en_bf.pdf
Rittersdorf, I. (2007). Gamma ray spectroscopy. https://websites.umich.edu/~ianrit/gammaspec.pdf
Ritz, M., Vaculíková, L., & The Czech Academy of Sciences. (2011). Application of infrared spectroscopy and chemometric methods to identification of selected minerals. Acta Geodynamica Et Geomaterialia, 47–58. https://www.researchgate.net/profile/L-Vaculikova/publication/266486725_Application_of_infrared_spectroscopy_and_chemometric_methods_to_identification_of_selected_minerals/links/54f8a70b0cf210398e96c708/Application-of-infrared-spectroscopy-and-chemometric-methods-to-identification-of-selected-minerals.pdf
SatisGeo. (2015). Instruments for Geophysics & Environment. Geraadpleegd op 6 maart 2024, van https://satisgeo.com/wp-content/uploads/2020/03/GS-512i-Manual.pdf
Schroeder, P. & University of Georgia. (2002). Infrared spectroscopy in Clay Science [Journal-article]. CMS Workshop Lectures, 11, 181–206. https://www.researchgate.net/profile/Paul-Schroeder-5/publication/237527451_Infrared_spectroscopy_in_clay_science/links/544a15ff0cf2f6388084ed7f/Infrared-spectroscopy-in-clay-science.pdf
Serra, O., Baldwin, J., & Quirein, J. (1980). Theory, interpretation, and practical applicatons of natural gamma ray spectroscopy. OnePetro. https://onepetro.org/SPWLAALS/proceedings/SPWLA-1980/All-SPWLA-1980/SPWLA-1980-Q/19466
Starkey, H., & C. Starkey, H. (1982). The Role of Clays in Fixing Lithium. In United States Government Printing Office, United States Department of the Interior, Geological Survey, & D. L. Peck, GEOLOGICAL SURVEY BULLETIN (Vols. 1278-F). https://pubs.usgs.gov/bul/1278f/report.pdf
Stringfellow, W. T., & Dobson, P. (2021). Technology for the Recovery of Lithium from Geothermal Brines. Energies (Basel), 14(20), 6805. https://doi.org/10.3390/en14206805
Thompson, A., Hauff, P. L., & Robitaille, A. J. (1999). Alteration Mapping in Exploration: Application of Short-Wave Infrared (SWIR) Spectroscopy. SEG Discovery (Print), 39, 1–27. https://doi.org/10.5382/segnews.1999-39.fea
Van Adrichem Boogaert, H.A., and W.F.P. Kouwe, comps., 1993, Stratigraphic nomenclature of the Netherlands, revision and update by Rijks Geologische Dienst (RGD) and Netherlands Oil and Gas Exploration and Production Association (NOGEPA): Mededelingen Rijks Geologische Dienst 50.
Velde, B., 1977, Clays and clay minerals in natural and synthetic systems: Amsterdam, Elsevier, 218 p

Wesseling, D. (2023). Characterising NaI(Tl) Scintillator Detectors for Gamma-ray Measurements: Evaluating Energy Resolution and Performance. Thesis. https://fse.studenttheses.ub.rug.nl/31162/1/thesis_final_s3812383.pdf
Xie, R., Zhao, Z., Xiong, T., Xie, X., Song, Q., & Fan, P. (2024). Review of the research on the development and utilization of clay-type lithium resources. Particuology, 87, 46–53. https://doi.org/10.1016/j.partic.2023.07.009
Z. Xu, B.C. Cornilsen, D.C. Popko,W.D. Pennington, J.R. Wood & J-Y Wang, Int. J. Vib. Spect., [www.irdg.org/ijvs] 5, 1, 4 (2001)
Zhao, H., Wang, Y., & Cheng, H. (2023). Recent advances in lithium extraction from lithium-bearing clay minerals. Hydrometallurgy, 217, 106025. https://doi.org/10.1016/j.hydromet.2023.106025
Zuo, K., Wang, H., Xiong, K., Chen, Y., & Cheng, H. (2022). Structural transformation and dehydroxylation of clay minerals in lithium-bearing clay. Journal Of Thermal Analysis And Calorimetry, 147(23), 13231–13237. https://doi.org/10.1007/s10973-022-11581-4

Appendix

Appendix 1

Mineral	**Formula**
Aleksandrovite	KCa7Sn2Li3Si12O36F2
Alumino-ottoliniite	NaLi(Mg3Al2) Si8O22(OH)2
Amblygonite	(LiNa)AlPO4(FOH)
Balestraite	KLi2V5+Si4O12
Balipholite	BaLiMg2Al3(Si2O6)2(OH)4
Baratovite	KCa7(Ti, Zr)2Li3Si12O36F2
Berezanskite	K2Li3(Ti, Zr, Sn)2(Si12O30)
Bertossaite	(Li, Na)2(Ca,Fe2+,Mn2+)Al4(PO4)4(OH,F)4
Bikitaite	(LiAlSi2)6·H2O)
Bityite	LiCaAl2(AlBeSi2O10) (OH)2
Borocookeite	LiAl4(BSi3O10) (OH)8
Brannockite	(K, Na)2Li3(Sn, Zr, Ti)2(Si12O30)
Bulgakite	Li2(Ca, Na) Fe2+Ti2(Si4O12)2O2(OH)4(F, O) (H2O)2
Ciprianiite	Ca4[(Th, U) (Li)2(Al)2(Si4B4O22) (OH, F)2
Clino-ferri-holmquistite	Li2(Mg3Fe23+) (Si8O22) (OH)2
Clino-ferro-ferri-holmquistite	Li2(Fe32+Fe23+) (Si8O22) (OH)2
Clinoferroholmquistite	(Li2Fe++3Al2) Si8O22(OH)2
Clinoholmquistite	(Li2Mg3Al2) Si8O22(OH)2
Colquiriite	Ca Li(AlF6)
Cookeite	LiAl14Si3O10(OH)8
Cryolithionite	Na3Li3(AlF6)2
Darapiosite	K (Na, K)2(Li, Zn, Fe)3(Mn, Zr, Y)2(Si12O30)
Darrellhenryite	Na(LiAl2) Al6(BO3)3Si6O18(OH)3O
Dellaventuraite	Na3(Mg2, Mn, Li, Ti) Si8O24
Dilithium	Li2Te
Diomignite	Li2B4O7
Dusmatovite	K (Na, O)2(Zn, Li)3(Mn2+, Y, Zr)2(Si12O30)
Elbaite	Na (Li Al)3Al6Si6O18(BO)3(OH)4
Eliseevite	LiNa1.5Ti2(H1.5Si4O12) O2 · 2H2O
Emeleusite	Li2Na4Fe2Si12O30
Ephesite	LiNaAl2(Al2Si2O10) (OH)2
Eucryptite	(LiAlSiO4)
Faizievite	K2Na(Ca6Na) Ti4Li6Si24O66F2
Ferri-clinoferroholmquistitee	Li2(Fe2+Fe3+) Si8O22(OH)2
Ferri-fluoro-leakeite	Na(Na2) (Mg2Fe23+Li) (Si8O22) F2
Ferri-leakeite	Na(Na2) (Mg2Fe23+Li) Si8O22(OH)2
Ferri-ottoliniite	(Na, Li) (Mg3Fe3+) Si8O22(OH)2
Ferripedizite	NaLi2(Fe3+2Mg2Li) Si8O22(OH)2
Ferrisicklerite	Li1-x(Fex3+Fe2+1-x) PO4

Ferriwhittakerite	Na(NaLi) (Mg2Fe3+Li) Si8O22(OH)2
Ferro-ferri-fluoro-leakeite	Na(Na2) (Fe22+Fe23+Li) (Si8O22) (F)2
Ferro-ferri-pedrizite	Na) (Li2) (Fe22+Fe23+Li) Si8O22(OH)2
Ferro-fluoro-leakeite'	NaNa2(Fe22+Al2Li) (Si8O22) F2
Ferro-holmquistite	Li2(Fe32+Al2) (Si8O22) (OH)2
Ferroleakeite	NaNa2(Fe2+)3(Fe3+)2Li(Si8O22) (OH)2
Ferro-pedrizite	NaLi2(Fe22+Al2Li) Si8O22(OH)2
Fluor-elbaite	Na(Li1.5Al1.5) Al6(Si6O18) (BO3)3(OH)3F
Fluor-liddicoatite	Ca(Li2Al) Al6(Si6O18) (BO3)3(OH)3F
Fluoro-ferroleakeite	NaNa2(Fe2+Fe3+Li) Si8O22F2
Fluoro-leakeite	NaNa2(Mg2Al2Li) (Si8O22) F2
Fluoro-Liddicoatite	Ca(Li2Al) Al6(BO3)3Si6)18(OH)3F
Fluoro-sodic-pedrizite	NaLi2(Mg2Al2Li) S5Si8O22F2
Footemineite	Ca2Mn2+Mn2+2Mn2+2Be4(PO4)6(OH)4•6H2O
Gainesite	Na (Na, K) (Be, Li) Zr2(PO4)4 · 1.5-2H2O
Garmite	CsLiMg2(Si4O10) F2
Gorbunovite	CsLi2(Ti, Fe) Si4O10(F, OH, O)2
Griceite	LiF
Griphite	Na4Li2Ca6(Mn2+, Fe2+, Mg)19Al8(PO4)24(F, OH)8
Hectorite	(Na0.3(Mg, Li)3Si4O10(OH)2)
Holmquistite	Li2(Mg3Al2) (Si8O22) (OH)2
Hsianghualite	Ca3Li2(Be3Si3O12) F2
Jadarite	(Na2OLi2O(SiO2)2(B2O3)3H2O)
Katayamalite	KLi3Ca7Ti2(SiO3)12(OH)2
Kupletskite-(Cs)	-(Cs) (Cs, K)2 Na (Mn, Fe2+, Li)7(Ti, Nb)2Si8O26(OH)4F
Lavinskyite	K (Li Cu) Cu6(Si4O11)2(OH)4
Leakeite	NaNa2(Mg2Fe3+2Li) Si8O22(OH)2
Lepidolite	K (Li Al)3(Al Si)4O10(FOH)2
Liberite	Li2BeSiO4
Liddicoatite	Ca(Li2Al) Al6(Si6O18) (BO3)3(OH)3(OH)
Lintisite	LiNa3Ti2(Si2O6)2O2 · 2H2O
Lithiomagnesite	Li2Mg(CO3)2
Lithiomarsturite	LiCa2Mn2Si5O14(OH)
Lithiophilite	LiMnPO3
Lithiophorite	(Al, Li) Mn O2(OH)2
Lithiophosphate	Li3PO4
Lithiotantite	Li (Ta, Nb)3O8
Lithiowodginite	LiTa3O8
Luanshiweiite	KLiAl1.5(Si3.5Al0.5) O10(OH, F)2
Lunijianlaite	Li0.7Al6.2(AlSi7O20) (OH, O)10
Magnesioclinoholmquistite	Li2(Mg, Fe2+)3Al2Si8O22(OH)2
Magnesioholmquistite	Li2(Mg, Fe2+)3Al2Si8O22(OH)2
Magnesioneptunite	KNa2Li (Mg, Fe)2Ti2Si8O24
Magnesiostaurolite	Mg (Mg, Li)3(Al, Mg)18Si8O44(OH)4
Manandonite	Li2Al4(Si2AlB) O10(OH)8

Mangani-dellaventuraite	Na(Na2) (MgMn23+LiTi4+) Si8O22O2
Manganoneptunite	Na2KLiMn22+Ti2Si8O24
Masutomilite	(K, Rb) (Li, Mn3+, Al)3(AlSi3O10) (F, OH)2
Mccrillisite	Na Cs (Be, Li) Zr2(PO4)4 · 1-2H2O
Montebrasite	(Li Al(PO4) (OH
Murakamiite	Ca2LiSi3O8(OH)
Nalipoite	NaLi2PO4
Nalivkinite	Li2Na (Fe2+, Mn2+)7Ti2Si8O26(OH)4F
Nambulite	(LiNa)Mn4Si5O14(OH)
Nanlingite	Na (Ca5Li) Mg12(AsO3)2[Fe(AsO3)6] F14
Nanpingite	Cs (Al, Mg, Fe2+, Li)2(Si3Al) O10(OH, F)2
Natromontebrasite	(Na, Li) Al(PO4) (OH, F)
Natronambulite	(Na, Li) (Mn, Ca)4Si5O14OH
Neptunite	Na2KLiFe22+Ti2Si8O24
Norrishite	KLiMn23+(Si4O10) O2
Olympite	Na5Li(PO4)2
Orlovite	KLi2Ti(Si4O10) OF
Oxo-mangani-leakeite	NaNa2(Mn43+Li) Si8O22O2
Pahasapaite	Li8(Ca, Li, K)10.5Be24(PO4)24 · 38H2O
Palermoite	(Li, Na)2(Sr, Ca) Al4(PO4)4(OH)4
Peatite-(beta)	-(beta) Li4Na12Y12(PO4)12(CO3)4(F, OH)8
Petalite	LiAlSi4O10
Pezzottaite	Cs(Be2Li) Al2Si6O18
Piergoritee	e (Al0.5, Fe3+0.5) (Li, Be)2Si6B8O36(OH, F)2
Polylithionite	KLi2Al(Si4O10) (F, OH)2
Potassiccarpholite	K (Li, Mn2+)2Al4(Si2O6)2(OH, F)8
Potassic-ferri-leakeite	K(Na2) (Mg2Fe23+Li) Si8O22(OH)2
Potassicleakeite	KNa2Mg2Fe3+2LiSi8O22(OH)2
Potassic-mangani-leakeite	(Na, K) (Na2) (Mg2Mn23+Li) Si8O22(OH)2
Punkaruaivite	LiTi2(HSi4O12) (OH)2 · H2O
Ramikite-(beta)	Li4(Na, Ca)12Y6Zr6(PO4)12(CO3)4O4[(OH), F]4
Rankamaite	(Na, K, Pb, Li)3(Ta, Nb, Al)11(O, OH)30
Rossmanite	(LiAl2) Al6(Si6O18) (BO3)3(OH)3(OH)
Saliotite	(Li, Na) Al3(AlSi3O10) (OH)5
Sicklerite	(Li (Mn, Fe) PO4)
Silinaite	NaLiSi2O5 · 2H2O
Simferite	Li (Mg, Fe3+, Mn3+)2(PO4)2
Simmonsite	Na2LiAlF6
Sodic-ferri-clinoferroholmquistite'	Na0.5(Li2) (Fe32+Fe23+) (Si8O22) (OH)2
Sodic-ferripedrizite	Na(LiNa) (Fe3+2Mg2Li) Si8O22(OH, F)2
Sogdianite	K(Na)2Li3(Zr, Fe, Ti)2[Si12O30]
Sokolovaite	CsLi2Al(Si4O10) F2
Soliotite	(LiNa)Al3(AlSi3O10) (OH5)
Spodumene	Li Al (SiO3)2
Sugilite	KNa2(Fe Mn Al)2Li3Si12O3

Swinefordite	Li (Al, Li, Mg)4((Si, Al)4O10)2(OH, F)4 · nH2O
Tainiolite	KLiMg2(Si4O10) F2
Tancoite	LiNa2Al (PO4) (HPO4) (OH)
Tanohataite	LiMn2(HSi3O9)
Tavorite	(LiFe3+(PO4) (OH))
Tiptopite	K2 (Na, Ca)2Li3Be6(PO4)6(OH)2 · H2O
Trilithionite	K(Li1.5Al1.5) (AlSi3O10) (F, OH)2
Triphylite	(LiFe2+PO4)
Virgilite	LiAlSi2O6
Voloshinite	Rb (LiAl1.5) (Al0.5Si3.5) O10F2
Walkerite	Ca16(Mg, Li)2(B13O17(OH)12)4Cl6·28H2O
Watatsumiite	Na2K Li (Mn2+, Fe2+)2V24+(Si8O24)
Wilancookite	(Ba, K, Na)8(Ba, Li)6Be24P24O96·32H2O
Zabuyelite	(Li2CO3)
Zektzerite	Li Na (Zr Ti H F) Si6O15
Zinnwaldite	K Li Fe Al (AlSi3) O10(OHF)2

Table A 1: Minerals containing lithium.

Appendix 2

SENIOR DRILLING FLUID	Amount
BARACARB 1200	25KG
BARACARB 150	25 KG
BARACARB 5	1 TON
BARACARB 5	25 KG
BARACARB 50	1 TON
BARACARB 50	25 KG
BARACARB 600	25 KG
BARAFLAKE C	50 LB
BARAFLAKE M	50 LB
BARAFLC IE - 513	25 KG
BARAKLEAN -648	1000 L
BARAVIS	50 LB
BARAVIS IE -568	1000 L
BAROFIBRE	25 LB
BAROFIBRE COARSE	40 LB
BDF -919	50 LB
CHEM,NF- M6 DEFOAMING AGENT	5 gal
CITRIC ACID	25 KG
DRILTREAT	5 GAL
EZ MUL NT	275 GAL
LIME	25 KG
NUOSEPT 78	25KG
SODA ASH	25 KG
SODIUM BICARBONATE	25 KG

Table A 2: Drilling fluid added to the well during drilling (Halliburton, 2023).

Appendix 3

sample ID	ref. ID	name	method	search name	rating
15821582	--	1582158200000 - averaged - averaged	NIR	usgs_all	96,61
	Kaolinite	Kaolinite_CM7_NIC4bb_RREF			96,61
	Montmorillonite	Montmorillonite_CM26_NIC4bc_RREF			96,4
	Kaolinite	Kaolinite_KGa-2_(pxl)_NIC4bbb_RREF			96,3
	Kaolinite	Kaolinite_KGa-2_(pxl)_NIC4b_RREF			95,86
	Lepidolite	Lepidolite_NMNH105538_NIC4cc_RREF			95,86
15831582	--	1583158200000 - averaged - averaged	NIR	usgs_all	97,58
	Kaolinite	Kaolinite_CM7_NIC4bb_RREF			97,58
	Kaolinite	Kaolinite_KGa-2_(pxl)_NIC4bbb_RREF			97,01
	Kaolinite	Kaolinite_CM5_NIC4bb_RREF			96,65
	Lepidolite	Lepidolite_NMNH105538_NIC4cc_RREF			96,64
	Kaolinite	Kaolinite_KGa-1_(wxl)_NIC4bb_RREF			96,57
15841582	--	1584158200000 - averaged - averaged	NIR	usgs_all	96,5
	Kaolinite	Kaolinite_CM7_NIC4bb_RREF			96,5
	Kaolinite	Kaolinite_KGa-2_(pxl)_NIC4bbb_RREF			95,78
	Lepidolite	Lepidolite_NMNH105538_NIC4cc_RREF			95,75
	Kaolinite	Kaolinite_CM5_NIC4bb_RREF			95,5
	Montmorillonite	Montmorillonite_CM26_NIC4bc_RREF			95,43
15851582	--	1585158200000 - averaged - averaged	NIR	usgs_all	98,12
	Illite	Illite_GDS4.2_Marblehead_ASDNGb_AREF			98,12
	Illite	Illite_IL105_(1Md)_BECKb_AREF			97,48
	Montmorillonite	Montmorillonite_SWy-1_NIC4bcc_RREF			94,35
	Chlorite	Chlorite_HS179.1B_ASDFRb_AREF			93,66
	Chlorite	Chlorite_HS179.2B_ASDFRb_AREF			93,22
15871582	--	1587158200000 - averaged - averaged	NIR	usgs_all	98,57
	Illite	Illite_IL105_(1Md)_BECKb_AREF			98,57
	Chlorite	Chlorite_HS179.1B_ASDFRb_AREF			98,08
	Chlorite	Chlorite_HS179.2B_ASDFRb_AREF			97,53
	Illite	Illite_GDS4.2_Marblehead_ASDNGb_AREF			97,51
	Chlorite	Chlorite_HS179.3B_ASDFRb_AREF			94,36
15881582	--	1588158200000 - averaged - averaged	NIR	usgs_all	98,62
	Illite	Illite_IL105_(1Md)_BECKb_AREF			98,62
	Chlorite	Chlorite_HS179.1B_ASDFRb_AREF			98,33
	Chlorite	Chlorite_HS179.2B_ASDFRb_AREF			97,88
	Illite	Illite_GDS4.2_Marblehead_ASDNGb_AREF			97,87
	Chlorite	Chlorite_HS179.3B_ASDFRb_AREF			94,83
15891582	--	1589158200000 - averaged - averaged	NIR	usgs_all	98,15
	Chlorite	Chlorite_HS179.1B_ASDFRb_AREF			98,15
	Illite	Illite_IL105_(1Md)_BECKb_AREF			97,88
	Chlorite	Chlorite_HS179.2B_ASDFRb_AREF			97,87
	Illite	Illite_GDS4.2_Marblehead_ASDNGb_AREF			97,18

	Chlorite	Chlorite_HS179.3B_ASDFRb_AREF			95,39
16821582	--	1682158200000 - averaged - averaged	NIR	usgs_all	98,93
	Illite	Illite_IL105_(1Md)_BECKb_AREF			98,93
	Illite	Illite_GDS4.2_Marblehead_ASDNGb_AREF			98,51
	Chlorite	Chlorite_HS179.1B_ASDFRb_AREF			96,94
	Chlorite	Chlorite_HS179.2B_ASDFRb_AREF			96,21
	Chlorite	Chlorite_HS179.3B_ASDFRb_AREF			91,9
16831582	--	1683158200000 - averaged - averaged	NIR	usgs_all	98,11
	Chlorite	Chlorite_HS179.2B_ASDFRb_AREF			98,11
	Chlorite	Chlorite_HS179.1B_ASDFRb_AREF			98,09
	Illite	Illite_GDS4.2_Marblehead_ASDNGb_AREF			97,38
	Illite	Illite_IL105_(1Md)_BECKb_AREF			97,3
	Chlorite	Chlorite_HS179.3B_ASDFRb_AREF			95,98
16841582	--	1684158200000 - averaged - averaged	NIR	usgs_all	98,25
	Illite	Illite_IL105_(1Md)_BECKb_AREF			98,25
	Illite	Illite_GDS4.2_Marblehead_ASDNGb_AREF			98,12
	Chlorite	Chlorite_HS179.1B_ASDFRb_AREF			97,39
	Chlorite	Chlorite_HS179.2B_ASDFRb_AREF			97
	Chlorite	Chlorite_HS179.3B_ASDFRb_AREF			93,47
16851582	--	1685158200000 - averaged - averaged	NIR	usgs_all	98,8
	Illite	Illite_IL105_(1Md)_BECKb_AREF			98,8
	Illite	Illite_GDS4.2_Marblehead_ASDNGb_AREF			98,54
	Chlorite	Chlorite_HS179.1B_ASDFRb_AREF			97,6
	Chlorite	Chlorite_HS179.2B_ASDFRb_AREF			97,11
	Chlorite	Chlorite_HS179.3B_ASDFRb_AREF			93,51
16861582	--	1686158200000 - averaged - averaged	NIR	usgs_all	98,27
	Illite	Illite_IL105_(1Md)_BECKb_AREF			98,27
	Chlorite	Chlorite_HS179.1B_ASDFRb_AREF			98,25
	Chlorite	Chlorite_HS179.2B_ASDFRb_AREF			97,85
	Illite	Illite_GDS4.2_Marblehead_ASDNGb_AREF			97,8
	Chlorite	Chlorite_HS179.3B_ASDFRb_AREF			95,02
16871582	--	1687158200000 - averaged - averaged	NIR	usgs_all	97,79
	Chlorite	Chlorite_HS179.1B_ASDFRb_AREF			97,79
	Chlorite	Chlorite_HS179.2B_ASDFRb_AREF			97,35
	Illite	Illite_IL105_(1Md)_BECKb_AREF			96,64
	Illite	Illite_GDS4.2_Marblehead_ASDNGb_AREF			95,53
	Chlorite	Chlorite_HS179.3B_ASDFRb_AREF			95,25
16911582	--	1691158200000 - averaged - averaged	NIR	usgs_all	98,7
	Illite	Illite_GDS4.2_Marblehead_ASDNGb_AREF			98,7
	Illite	Illite_IL105_(1Md)_BECKb_AREF			97,68
	Chlorite	Chlorite_HS179.1B_ASDFRb_AREF			94,91
	Chlorite	Chlorite_HS179.2B_ASDFRb_AREF			94,64
	Montmorillonite	Montmorillonite_SWy-1_NIC4bcc_RREF			92,02
16921582	--	1692158200000 - averaged - averaged	NIR	usgs_all	99,1
	Illite	Illite_GDS4.2_Marblehead_ASDNGb_AREF			99,1

	Illite	Illite_IL105_(1Md)_BECKb_AREF			97,14
	Chlorite	Chlorite_HS179.2B_ASDFRb_AREF			96,18
	Chlorite	Chlorite_HS179.1B_ASDFRb_AREF			95,72
	Chlorite	Chlorite_HS179.3B_ASDFRb_AREF			93,4
15931582	--	1593158200000 - averaged - averaged	NIR	usgs_all	98,52
	Illite	Illite_IL105_(1Md)_BECKb_AREF			98,52
	Chlorite	Chlorite_HS179.1B_ASDFRb_AREF			98,29
	Illite	Illite_GDS4.2_Marblehead_ASDNGb_AREF			97,93
	Chlorite	Chlorite_HS179.2B_ASDFRb_AREF			97,84
	Chlorite	Chlorite_HS179.3B_ASDFRb_AREF			94,79
15941582	--	1594158200000 - averaged - averaged	NIR	usgs_all	98,07
	Chlorite	Chlorite_HS179.1B_ASDFRb_AREF			98,07
	Illite	Illite_IL105_(1Md)_BECKb_AREF			98
	Illite	Illite_GDS4.2_Marblehead_ASDNGb_AREF			97,68
	Chlorite	Chlorite_HS179.2B_ASDFRb_AREF			97,61
	Chlorite	Chlorite_HS179.3B_ASDFRb_AREF			94,69
15951582	--	1595158200000 - averaged - averaged	NIR	usgs_all	96,98
	Illite	Illite_GDS4.2_Marblehead_ASDNGb_AREF			96,98
	Illite	Illite_IL105_(1Md)_BECKb_AREF			96,23
	Chlorite	Chlorite_HS179.1B_ASDFRb_AREF			93,81
	Chlorite	Chlorite_HS179.2B_ASDFRb_AREF			93,34
	Illite	Illite_GDS4_Marblehead_ASDNGb_AREF			91,23
15961582	--	1596158200000 - averaged - averaged	NIR	usgs_all	98,02
	Illite	Illite_GDS4.2_Marblehead_ASDNGb_AREF			98,02
	Illite	Illite_IL105_(1Md)_BECKb_AREF			96,83
	Chlorite	Chlorite_HS179.1B_ASDFRb_AREF			94,69
	Chlorite	Chlorite_HS179.2B_ASDFRb_AREF			94,53
	Illite	Illite_GDS4_Marblehead_ASDNGb_AREF			92,5
15981582	--	1598158200000 - averaged - averaged	NIR	usgs_all	98,35
	Chlorite	Chlorite_HS179.1B_ASDFRb_AREF			98,35
	Chlorite	Chlorite_HS179.2B_ASDFRb_AREF			97,82
	Illite	Illite_IL105_(1Md)_BECKb_AREF			97,45
	Illite	Illite_GDS4.2_Marblehead_ASDNGb_AREF			96,49
	Chlorite	Chlorite_HS179.3B_ASDFRb_AREF			95,39
15991582	--	1599158200000 - averaged - averaged	NIR	usgs_all	98,48
	Illite	Illite_IL105_(1Md)_BECKb_AREF			98,48
	Illite	Illite_GDS4.2_Marblehead_ASDNGb_AREF			98,31
	Chlorite	Chlorite_HS179.1B_ASDFRb_AREF			97,67
	Chlorite	Chlorite_HS179.2B_ASDFRb_AREF			97,18
	Chlorite	Chlorite_HS179.3B_ASDFRb_AREF			93,76
16981582	--	1698158200000 - averaged - averaged	NIR	usgs_all	97,65
	Chlorite	Chlorite_HS179.1B_ASDFRb_AREF			97,65
	Chlorite	Chlorite_HS179.2B_ASDFRb_AREF			97,36
	Illite	Illite_IL105_(1Md)_BECKb_AREF			96,55
	Illite	Illite_GDS4.2_Marblehead_ASDNGb_AREF			95,82

	Chlorite	Chlorite_HS179.3B_ASDFRb_AREF			95,43
16991582	--	1699158200000 - averaged - averaged	NIR	usgs_all	98,78
	Illite	Illite_GDS4.2_Marblehead_ASDNGb_AREF			98,78
	Illite	Illite_IL105_(1Md)_BECKb_AREF			98,7
	Chlorite	Chlorite_HS179.1B_ASDFRb_AREF			96,66
	Chlorite	Chlorite_HS179.2B_ASDFRb_AREF			96,15
	Chlorite	Chlorite_HS179.3B_ASDFRb_AREF			91,99
17001582	--	1700158200000 - averaged - averaged	NIR	usgs_all	94,56
	Kaolinite	Kaolinite_GDS11_lt63um_NIC4bb_RREF			94,56
	Kaolinite	Kaolinite_CM3_NIC4aa_RREF			94,38
	Kaolinite	Kaolinite_CM7_NIC4bb_RREF			94,17
	Lepidolite	Lepidolite_NMNH105538_NIC4cc_RREF			93,82
	Kaolinite	Kaolinite_KGa-1_(wxl)_NIC4bb_RREF			93,03
17021582	--	1702158200000 - averaged - averaged	NIR	usgs_all	98,18
	Chlorite	Chlorite_HS179.1B_ASDFRb_AREF			98,18
	Chlorite	Chlorite_HS179.2B_ASDFRb_AREF			97,93
	Illite	Illite_IL105_(1Md)_BECKb_AREF			97,14
	Illite	Illite_GDS4.2_Marblehead_ASDNGb_AREF			96,73
	Chlorite	Chlorite_HS179.3B_ASDFRb_AREF			95,87
17031582	--	1703158200000 - averaged - averaged	NIR	usgs_all	98,46
	Illite	Illite_IL105_(1Md)_BECKb_AREF			98,46
	Chlorite	Chlorite_HS179.1B_ASDFRb_AREF			97,93
	Illite	Illite_GDS4.2_Marblehead_ASDNGb_AREF			97,68
	Chlorite	Chlorite_HS179.2B_ASDFRb_AREF			97,23
	Chlorite	Chlorite_HS179.3B_ASDFRb_AREF			93,56
15901582	--	1590158200000 - averaged - averaged	NIR	usgs_all	96,88
	Illite	Illite_GDS4.2_Marblehead_ASDNGb_AREF			96,88
	Illite	Illite_IL105_(1Md)_BECKb_AREF			95,52
	Kaolinite	Kaolinite_GDS11_lt63um_NIC4bb_RREF			92,05
	Chlorite	Chlorite_HS179.1B_ASDFRb_AREF			91,75
	Illite	Illite_GDS4_Marblehead_ASDNGb_AREF			91,65
15921582	--	1592158200000 - averaged - averaged	NIR	usgs_all	98,5
	Illite	Illite_IL105_(1Md)_BECKb_AREF			98,5
	Illite	Illite_GDS4.2_Marblehead_ASDNGb_AREF			98,37
	Chlorite	Chlorite_HS179.1B_ASDFRb_AREF			96,97
	Chlorite	Chlorite_HS179.2B_ASDFRb_AREF			96,35
	Chlorite	Chlorite_HS179.3B_ASDFRb_AREF			92,36
16931582	--	1693158200000 - averaged - averaged	NIR	usgs_all	98,44
	Illite	Illite_GDS4.2_Marblehead_ASDNGb_AREF			98,44
	Illite	Illite_IL105_(1Md)_BECKb_AREF			96,89
	Chlorite	Chlorite_HS179.1B_ASDFRb_AREF			94,17
	Chlorite	Chlorite_HS179.2B_ASDFRb_AREF			94,16
	Illite	Illite_GDS4_Marblehead_ASDNGb_AREF			91,78
16941582	--	1694158200000 - averaged - averaged	NIR	usgs_all	97,29
	Illite	Illite_GDS4.2_Marblehead_ASDNGb_AREF			97,29

	Kaolinite	Kaolinite_GDS11_lt63um_NIC4bb_RREF			94,71
	Kaolinite	Kaolinite_CM3_NIC4aa_RREF			94,58
	Kaolinite	Kaolinite_CM7_NIC4bb_RREF			94,46
	Illite	Illite_GDS4_Marblehead_ASDNGb_AREF			94,32
16951582	--	1695158200000 - averaged - averaged	NIR	usgs_all	96,81
	Kaolinite	Kaolinite_CM7_NIC4bb_RREF			96,81
	Kaolinite	Kaolinite_GDS11_lt63um_NIC4bb_RREF			96,62
	Kaolinite	Kaolinite_CM3_NIC4aa_RREF			96,34
	Lepidolite	Lepidolite_NMNH105538_NIC4cc_RREF			95,87
	Kaolinite	Kaolinite_KGa-2_(pxl)_NIC4bbb_RREF			95,68
16961582	--	1696158200000 - averaged - averaged	NIR	usgs_all	96,92
	Kaolinite	Kaolinite_CM7_NIC4bb_RREF			96,92
	Kaolinite	Kaolinite_GDS11_lt63um_NIC4bb_RREF			96,5
	Kaolinite	Kaolinite_CM3_NIC4aa_RREF			96,34
	Lepidolite	Lepidolite_NMNH105538_NIC4cc_RREF			96,05
	Kaolinite	Kaolinite_KGa-2_(pxl)_NIC4bbb_RREF			95,87

Table A 3 Spectragryph classification of all sample spectra

Appendix 4

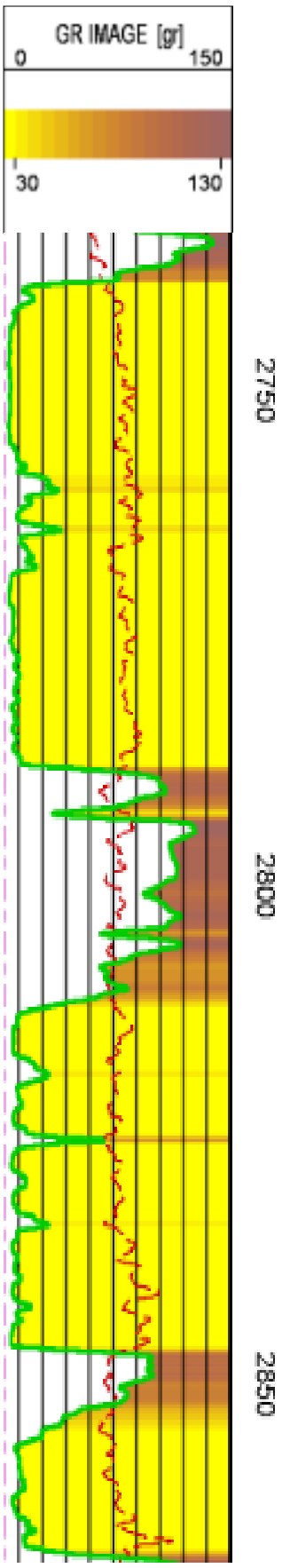

Table A 4 GR well logs of defined interval (Baker Hughes, 2023)